https://doi.org/10.5194/egusphere-2026-2178
Preprint. Discussion started: 21 July 2026

Examining anthropogenic CO_2 emission inventories over the Greater Tokyo Area using in situ observations and high-resolution atmospheric simulation

Zhenglun Yang[1], Yukio Terao[1], Thomas Lauvaux[2], Tomohiro Oda[3,4], Charbel Abdallah[2], Masahide Nishihashi[5], Makoto Saito[1], Hirofumi Ohyama[1], Shigeyuki Ishidoya[6], Hirofumi Sugawara[7], Toshinobu Machida[1], Motoki Sasakawa[1], and Yasunori Tohjima[1]

[1]Earth System Division, National Institute for Environmental Studies, Tsukuba, 305-8506, Japan
[2]Groupe de Spectrométrie Moléculaire et Atmosphérique (GSMA), Université de Reims Champagne-Ardenne, UMR CNRS 7331, Reims, 51687, France
[3]Earth from Space Institute, Universities Space Research Association (USRA), Washington, DC, 20024, USA
[4]Department of Atmospheric and Oceanic Science, University of Maryland, College Park, MD, 20742, USA
[5]Department of Observation and Data Assimilation Research, Meteorological Research Institute, Tsukuba, 305-0052, Japan
[6]Global Zero Emission Research Center, National Institute of Advanced Industrial Science and Technology (AIST), Tsukuba, 305-8569, Japan
[7]Department of Earth and Ocean Sciences, National Defense Academy of Japan, Yokosuka, 239-8686, Japan

Correspondence to: Zhenglun Yang (yang.zhenglun@nies.go.jp) and Yukio Terao (yterao@nies.go.jp)

Abstract. Cities are major sources of greenhouse gas emissions, and combining activity-based inventories with atmospheric constraints can support science-based mitigation at subnational levels. We implement high-resolution WRF-Chem simulations over the Greater Tokyo Area (GTA) using five anthropogenic emission inventories (MOSAIC, ODIAC, EDGAR, CAMS-GLOB-ANT, and GCP-GridFED) and examine CO_2 concentrations at four sites. Using observations from the summit of Mt. Fuji as a background reference, we derive GTA CO_2 enhancements (ΔCO_2). The simulations reproduce most observed ΔCO_2 variability and the relationship between elevated ΔCO_2 and transport from the urban core and the Tokyo Bay, while showing differences in ΔCO_2 amplitudes due to five inventories. The four observation sites represent different GTA subregions, providing complementary constraints on inventory spatial patterns and highlighting the importance of site selection in urban assessments. High simulated ΔCO_2 at Tsukuba is largely attributable to stronger northern suburban emissions in MOSAIC and ODIAC, whereas high ΔCO_2 at Yoyogi in ODIAC and GridFED is attributable to stronger nearby urban-core emissions. CAMS-GLOB-ANT and GridFED overestimate ΔCO_2 at Yokosuka because of large emissions along the Tokyo Bay. EDGAR shows the lowest bias, although its spatial distribution is coarse and diffuse compared with MOSAIC and ODIAC. Anthropogenic CO_2 is best reproduced by EDGAR and MOSAIC, though this result is strongly influenced by Yoyogi. Corrected total GTA CO_2 emissions of inventories range from 60.2 to 81.1 Tg C yr^{-1}. These results show where inventories diverge within a megacity and provide a practical benchmark for improving urban CO_2 inventories and future urban emission monitoring.

https://doi.org/10.5194/egusphere-2026-2178
Preprint. Discussion started: 21 July 2026

1 Introduction

Human activities especially fossil fuel combustion have led to a continuous increase in atmospheric CO_2 concentrations over the past century (Friedlingstein et al., 2022; IPCC, 2021). Anthropogenic CO_2 emissions are predominantly concentrated within metropolitan regions, owing to high population density, high energy consumption, intensive traffic, and substantial industrial activity (Crippa et al., 2021; IEA, 2022; Ribeiro et al., 2019). With ongoing urbanization, cities are recognised as major emission hotspots and key targets of climate policy (Liotta et al., 2023; Winkler et al., 2023), therefore quantifying urban scale emissions and their variability is essential (Kiel et al., 2021; Yap et al., 2025). However, robust estimation at the urban scale remains challenging because emission sources are highly heterogeneous in space and time (Liu et al., 2024), atmospheric transport in urban areas is complex, and observational constraints are often sparse in both space and time (Vardag and Maiwald, 2024). More fundamentally, urban emissions estimation also faces a reporting challenge because city inventories are often developed using different accounting frameworks, boundary definitions, source coverage, while self-reported inventories may omit particular fuels or source types or estimate transportation emissions differently (Gurney et al., 2021).

Bottom-up emission inventories serve as the foundational data set for estimating greenhouse gas emissions at various scales from global to urban. However, despite methodological progress, large uncertainties remain, especially in urban areas (Arioli et al., 2020; Gately and Hutyra, 2017; Han et al., 2020b, a; Oda et al., 2019). These uncertainties arise from differences in activity data, emission factors, sector definitions, boundary treatments, and the spatial and temporal resolution at which inventories are compiled (Ahn et al., 2023; Chen et al., 2020; Han et al., 2020a). Variations in spatial proxies or allocation schemes—for example, how industrial zones or power plants are located—can lead to distinct urban emission patterns even when national totals are consistent (Geng et al., 2017; Thorpe et al., 2023; Zheng et al., 2017). Recent urban modeling studies have confirmed that such structural differences among inventories can produce substantial spread in simulated CO_2 fields, even when the same transport model and meteorology are used (Lian et al., 2023; Yang et al., 2020). Urban inversion studies further indicate that uncertainties in the spatial and temporal distribution of fossil-fuel emissions can rival or exceed other components of the error budget at the urban scale (Lauvaux et al., 2016, 2020). These issues underscore the necessity of evaluating and comparing several emission inventories to understand the urban CO_2 estimates.

Atmospheric observations of CO_2 concentrations provide an independent constraint for estimating of CO_2 emissions. High-frequency in situ measurements, tower networks, ground-based column observations, aircraft profiles, and satellite products have all been used to evaluate urban CO_2 signals and to infer city-scale emissions (e.g., Bisht et al., 2025; Che et al., 2024a, b; Feng et al., 2024; Kim et al., 2025; Taquet et al., 2024). Long-term and continuous CO_2 observations capture a wide range of meteorological conditions and emission patterns, allowing robust evaluation of seasonal and spatial variability (Lauvaux et al., 2016; Lian et al., 2019; Sargent et al., 2018). Observation networks that include urban and suburban or background sites are particularly useful, because they help to show how the spatial allocation of emissions and the representation of source locations in the inventories affect the concentration changes observed at different sites (e.g., Barkley et al., 2023; Karion et al., 2021; Lian et al., 2023). Integrated observation–model analyses are therefore important for improving the consistency and reliability of urban scale emission inventories. Building on these strengths, recent assessment frameworks increasingly emphasize the complementary use of activity-based and atmospheric-based approaches, with hybrid frameworks offering a promising pathway towards more relevant and accurate emissions information for decision making at subnational scales such as cities (NASEM, 2022). This perspective is consistent with the IG3IS Urban Greenhouse Gas Emission Observation and Monitoring Good Research Practice Guidelines, which integrate inventory information, process models, atmospheric observations, and atmospheric modelling to support urban greenhouse gas assessment and decision making (WMO, 2022, 2025).

For the observation-model frameworks, the Weather Research and Forecasting model coupled with Chemistry (WRF-Chem) has been applied in several cities worldwide (Abdallah et al., 2024; Alberti et al., 2025; Bisht et al., 2025; Callewaert et al., 2025; Feng et al., 2016; Lian et al., 2023; Nerobelov et al., 2023; Zhao et al., 2023). In Los Angeles, WRF-Chem evaluations highlighted the need for ~1 km $FFCO_2$ emissions modelling, since coarser-resolution emissions can overestimate observational

https://doi.org/10.5194/egusphere-2026-2178
Preprint. Discussion started: 21 July 2026

constraints on emission estimates (Feng et al., 2016). Over the Paris, multi-site continuous CO_2 measurements combined with WRF-Chem enabled long-term emission estimates and detected clear changes during the COVID-19 period (Abdallah et al., 2024; Lian et al., 2023). In St. Petersburg, column-average CO_2 was evaluated using WRF-Chem simulation and EM27/SUN observations, showing strong temporal skill but also sensitivity to boundary conditions and background treatment (Nerobelov et al., 2023). In São Paulo, WRF-Chem CO_2 simulations were evaluated against in situ measurements from the METROCLIMA network and OCO-2 XCO_2, demonstrating strong skill in reproducing seasonal CO_2 variability in a tropical megacity (Alberti et al., 2025).

The Greater Tokyo Area (GTA) is one of the world's largest megacities and serves as a paradigmatic example of many urban carbon challenges. Recent studies have combined diverse atmospheric observation types—ground-based column FTIR, tall tower in situ measurements, aircraft campaigns, and satellite products—with regional and global transport models to quantify anthropogenic CO_2 and to test inventory or modelling choices over Tokyo. Column observations have been used to infer GTA emissions and to highlight the sensitivity to sampling strategy and background treatment (Ohyama et al., 2023). A global high-resolution framework with tagged tracers and the tower observation isolated Tokyo-origin CO_2 signals and examined the wind-regime dependence of inferred fluxes (Yamada et al., 2025). High-resolution WRF-GHG simulations over Kanto have explored how boundary conditions, spatial resolution, and inventory inputs shape urban CO_2 fields, emphasizing the role of configuration choices for receptor-level signals (Bisht et al., 2023, 2025). Collectively, these efforts demonstrate clear progress but remain limited by short analysis windows, single-site or campaign-based sampling, and a focus on one inventory or one configuration at a time. Systematic kilometer-scale evaluations that compare multiple bottom-up inventories under a common high-resolution modelling framework and across several receptor sites remain scarce.

In this study we performed high-resolution CO_2 simulations over the GTA using WRF-Chem for one year and compared it with continuous CO_2 observations from four tower sites located in the urban and suburban areas. Five widely used bottom-up inventories were used for the simulations under the same model setup to examine their spatial and temporal variations in the simulated CO_2 fields and biases. The objective of this study is to evaluate how each inventory reproduces observed CO_2 patterns across multiple sites, quantify cross-inventory spatial differences in the simulated fields, and identify the main contributors to model–observation differences, with emphasis on emission distribution versus meteorological effects. This design provides a consistent basis for assessing urban CO_2 inventories and for informing future urban scale carbon monitoring.

https://doi.org/10.5194/egusphere-2026-2178
Preprint. Discussion started: 21 July 2026

2 Methodology

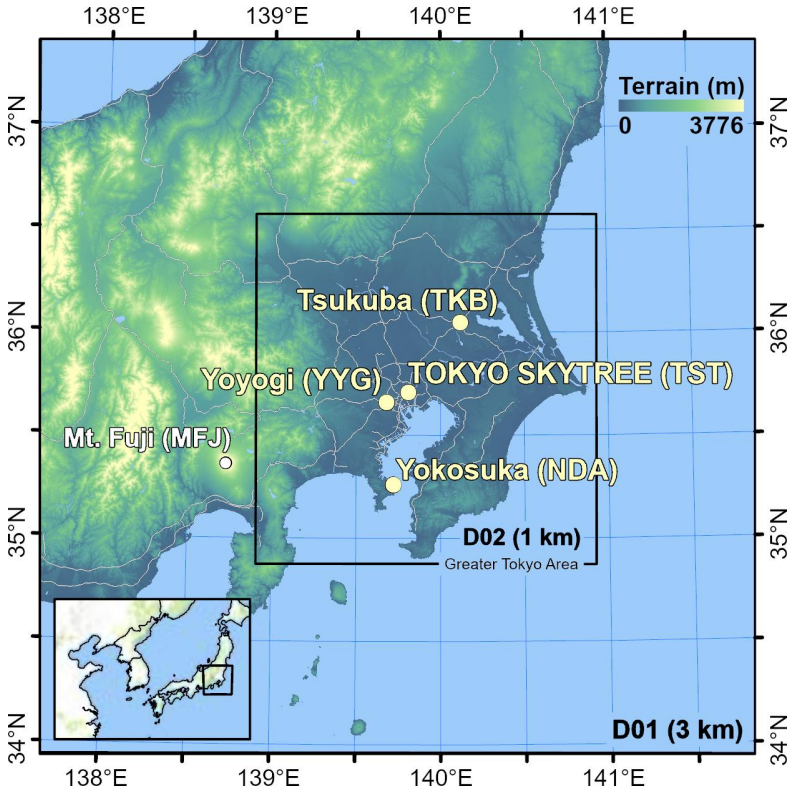

Figure 1: Locations of CO_2 observation sites and WRF-Chem domains over the GTA. Yellow circles indicate the locations of four CO_2 tower sites (TKB, TST, YYG, NDA), and a white circle marks observation site at the summit of Mt. Fuji (MFJ). The simulation uses two nested domains with horizontal resolutions of 3 km (domain 1) and 1 km (domain 2). Terrain elevation is generated using the AW3D30 (30 m) dataset provided by JAXA.

Figure 1 shows the study area, the atmospheric observation sites (Section 2.1), and the nested WRF-Chem domains used in this study. The outer WRF-Chem domain (d01) covers the Kanto region, while the inner domain (d02) resolves the Greater Tokyo Area (GTA) at higher spatial resolution (Section 2.2). The GTA includes Tokyo and the surrounding 7 prefectures of Kanagawa, Saitama, Chiba, Ibaraki, Tochigi, Gunma, and Yamanashi, covering approximately 36,900 km² and hosting more than 44 million residents (2020 Population Census: https://www.stat.go.jp/english/data/kokusei/index.html). It is also one of the world's largest metropolitan economies, with an average regional GDP of about USD 1.68 trillion during 2016–2020 (National Accounts of Japan: https://www.esri.cao.go.jp/jp/sna/menu.html). The region contains dense urban and industrial areas, with major point source emissions concentrated around Tokyo Bay, as well as surrounding forests and mixed rural landscapes that introduce varying biogenic CO_2 fluxes. Against this backdrop, we conduct an intercomparison of five widely used anthropogenic CO_2 emission inventories (Section 2.3) using otherwise identical WRF-Chem simulations and evaluate the simulated CO_2 fields against atmospheric observations from the sites shown in Fig. 1. The analysis covers the full year of 2018.

https://doi.org/10.5194/egusphere-2026-2178
Preprint. Discussion started: 21 July 2026

2.1 Atmospheric CO_2 observations

We have performed continuous measurements of CO_2 mole fraction at four sites over the GTA (Fig. 1): TOKYO SKYTREE (TST) and Yoyogi (YYG) in the urban core, Tsukuba (TKB) in the northern suburban area, and Yokosuka (NDA) on the western coast of Tokyo Bay. Together, these sites capture urban, suburban, and coastal representing and the key inflow/outflow pathways relevant for interpreting inventory-driven differences in simulated CO_2. The characteristics of the four observation sites are as follows:

- TKB is located 50 km northeast of Tokyo in a rural area (36.05°N, 140.12°E). Measurements were performed on the rooftop of the tallest building in the NIES campus (32 m above ground level). It is often downwind of the Tokyo core during summer southerlies and upwind during winter northerlies, providing valuable information on the regional CO_2 baseline.
- TST is located on a 634 m-high broadcasting tower in central Tokyo (35.71°N, 139.81°E). The instruments and air inlet were installed at approximately 250 m above ground level. The observation height generally lies within the daytime mixed layer throughout most of the year; even in winter, the mixed layer often extends above 200 m (Nakajima et al., 2018). TST data from February 22 to April 26, 2018, were excluded from the analysis due to contamination of the sampling line.
- YYG is an urban residential site in central Tokyo (35.66°N, 139.68°E), surrounded by buildings with an average height of 9 m (Hirano et al., 2015; Ishidoya et al., 2020; Sugawara et al., 2021). Air samples were collected from an inlet installed on a roof-top tower of Tokai University (37 m above ground level) and analysed inside the building. The site is strongly influenced by local traffic and residential emissions and provides high CO_2 concentration data frequently reflecting neighborhood–scale variability.
- NDA is located ~50 km south of Tokyo in a coastal urban environment (35.26°N, 139.72°E). Measurements were performed on the rooftop of the building in the National Defense Academy of Japan campus on the hill (13 m above ground level and 99 m above sea level). The location is affected by carbon dioxide transport from northern urban and the Tokyo Bay area, as well as by ocean air from the south, especially under winter northerly winds. We began the measurements at NDA on February 20, 2018, thus no data was available before that.

All sites were equipped with wavelength-scanned cavity ring-down spectrometers (WS-CRDS; G2401, Picarro). Air samples were taken from an air inlet using a diaphragm pump, then dehumidified by passing through a Nafion dryer (MD-050-72S; Perma Pure), and introduced into the WS-CRDS at a flow rate of 100 mL/min. Three standard gases with different CO_2 concentrations were used to calibrate the WS-CRDS every 50 h. The CO_2 concentrations were determined against the National Institute for Environmental Studies (NIES) 09 scales (Machida et al., 2011). The analytical reproducibility of 1-min averaged data, defined as the standard deviation of 1-min averaged standard gas measurements, was approximately ±0.02 ppm. Hourly average data were used for comparison with the simulations, consistent with the temporal resolution of the simulation outputs. Our high accuracy multi-site observational network, spanning both densely urbanized and suburban regions, provides a robust foundation for evaluating simulated CO_2 spatial gradients and transport processes across the Tokyo megacity. Seasonal winds are governed by the East Asian monsoon. In winter, frequent northwesterlies linked to the Siberian High promote outflow from inland to the Pacific (Ishidoya et al., 2020; Itoh et al., 2016). In summer, southerly winds associated with the Pacific subtropical high bring maritime air into the city. These contrasting regimes drive strong seasonal changes in transport and boundary-layer depth, which in turn affect the dispersion and accumulation of CO_2 over the GTA.

We also used measurements of CO_2 mole fraction at the top of Mt. Fuji (MFJ, 35.21° N, 138.43° E; 3776 m a.s.l.) as a reference site for the GTA. The MFJ data was representative of free-tropospheric air masses and free from strong local anthropogenic or biogenic influences (Nomura et al., 2017). Night-time data were used because the MFJ observation period was set during the night to avoid local daytime influences from air-mass transport around Mt. Fuji, allowing the measurements to better represent the background reference. We used the MFJ site as the regional background because it is close to the GTA but located at high elevation with weak local sources. The daily CO_2 mole fractions at MFJ were derived from night-time measurements between 22:00 and 23:00 JST.

https://doi.org/10.5194/egusphere-2026-2178
Preprint. Discussion started: 21 July 2026

2.2 WRF-Chem atmospheric CO_2 simulation

We used the WRF-Chem CO_2 (Lauvaux et al., 2012), which was based on WRF-Chem version 3.9.1 but modified for passive tracers, to simulate atmospheric CO_2 over the GTA. In our model, CO_2 was treated as a passive tracer without chemical reactions or feedback on meteorology. A two-domain nested configuration was designed to capture both regional-scale transport and urban-scale concentration variability on the Kanto Plain in eastern Japan (Fig. 1). The outer domain (d01) covered eastern Japan at a horizontal resolution of 3 km, while the inner domain (d02) focused on the GTA with a resolution of 1 km. The domain spans densely built urban districts around Tokyo Bay and transitions to suburban and rural areas toward the north and west, where low mountains rise along the Kanto boundary. Both domains employed 51 vertical levels extending from the surface to 100 hPa, with finer resolution in the planetary boundary layer to better represent near-surface mixing and vertical transport. A summary of the WRF-Chem model configuration and physical parameterizations is provided in Table 1.

Table 1. A summary of the model configuration.

Component	Description	Reference(s)
Initial and lateral boundary conditions	Meteorology: MSM–GPV Soil: NCEP GDAS/FNL 0.25°	JMA (2019) NCEP (2015)
Number of vertical layers	51 layers	
Land use data	Veg_jstream	Chatani et al. (2018)
Planetary boundary layer (PBL)	Mellor-Yamada-Janjić (MYJ) scheme	Janjić (1994)
Land surface model (LSM)	Rapid Update Cycle (RUC) model	Smirnova et al. (2016)
Microphysics	Thompson scheme	Thompson et al. (2008)
Cumulus parameterization	Kain–Fritsch scheme (only d01)	Kain (2004)
Shortwave and Longwave Radiation	RRTMG scheme	Iacono et al. (2008)

Our WRF-Chem was driven by meteorological fields taken from the Japan Meteorological Agency (JMA) Meso-Scale Model Grid Point Value (MSM–GPV) dataset, providing realistic representations of regional circulation patterns and boundary-layer processes. Soil and land-surface initial conditions were initialized using the NCEP GDAS/FNL (Final) 0.25 Degree Global Tropospheric Analyses and Forecast Grids (NCEP, 2015). The Mellor–Yamada–Janjic (MYJ) planetary boundary-layer scheme was used in combination with the Rapid Update Cycle (RUC) land-surface model. The performance of both models in reproducing wind and temperature structures over the Tokyo area was reported by Ohyama et al. (2023). Radiation and microphysics processes followed the default WRF-Chem physics suite optimized for mesoscale meteorological applications. The simulation period covered the entire year of 2018, enabling an assessment of seasonal variations of CO_2. The model produced hourly outputs for all variables, ensuring temporal consistency with the observational data. This setup provides a balance between high spatial resolution required for urban emission gradients and computational efficiency for long-term simulations.

In the simulations, the boundary conditions of CO_2 were obtained from the CAMS global inversion-optimized greenhouse gas flux and concentration product version v23r3 (Chevallier et al., 2010; Copernicus Atmosphere Monitoring Service, 2020). The v23r3 product provides global three-hourly CO_2 mixing ratios at a horizontal resolution of 1.4° × 0.7°, including both surface fluxes and three-dimensional concentration fields. These concentration fields were spatially and temporally interpolated to the outer model boundaries of the WRF-Chem simulation to represent realistic background inflow. This treatment allows synoptic-scale variability in background CO_2 to be included, improving the ability of the regional simulations to reproduce observed atmospheric CO_2 patterns.

https://doi.org/10.5194/egusphere-2026-2178
Preprint. Discussion started: 21 July 2026

2.3 Anthropogenic CO_2 emission inventories

Table 2. Emission inventories used in the WRF-Chem CO_2 simulations.

Dataset	Covered region	Time and spatial resolution	Approach	Reference
MOSAIC	Japan	Monthly 1km x 1km	Bottom-up calculation and emission modelling using country/region specific data	Saito et al. (2022)
ODIAC	Global	Monthly 1km x 1km	Disaggregation of country emissions using point-source information, satellite-derived nighttime lights, and aircraft and ship fleet tracks	Oda and Maksyutov (2015)
EDGAR	Global	Monthly 0.1° × 0.1°	Bottom-up calculation and sector-specific gridding using harmonized energy statistics, activity data, emission factors, and spatial proxies	Crippa et al. (2023)
CAMS-GLOB-ANT	Global	Monthly 0.1° × 0.1°	Global gridded emissions based on EDGAR, extrapolated to recent years using CEDS, and combined with CAMS temporal profiles and ship emissions	Soulie et al. (2024)
GCP-GridFED	Global	Monthly 0.1° × 0.1°	Scaling of EDGAR monthly gridded emissions to match national annual emissions from the Global Carbon Budget	Jones et al. (2021)

We used five anthropogenic CO_2 emission inventories for comparison (Table 2). These inventories include one high-resolution regional emission dataset for Japan (MOSAIC) and four widely used global bottom-up datasets (ODIAC, EDGAR, CAMS-GLOB-ANT, and GCP-GridFED). The inventories employed are:

(1) Multiscale Overlap Scheme for Analysing national Inventory of anthropogenic CO_2 (MOSAIC), a high-resolution anthropogenic emissions dataset specifically developed for Japan, with a spatial resolution of approximately 1 km × 1 km (Saito et al., 2022). It utilizes a range of national statistical datasets—such as sectoral energy consumption, road networks, and building footprints—to spatially allocate fossil fuel CO_2 emissions across the country. The dataset includes monthly emissions estimates for eight sectors: electricity generation, industrial and commercial activities, residential sources, road transport, civil aviation, waterborne navigation, waste incineration, and agricultural machinery. In this study, we employed the 2015 version of MOSAIC, which was the only available release at the time.

(2) Open-Data Inventory for Anthropogenic Carbon dioxide (ODIAC) version 2023 (Oda and Maksyutov, 2015), which provides global fossil fuel CO_2 emissions at a high spatial resolution of 1 km × 1 km over land by combining power plant profiles (emission intensity and location) and satellite-observed nighttime lights (Oda et al., 2018).

(3) Emissions Database for Global Atmospheric Research (EDGAR) version 8.0 (Crippa et al., 2023), provides global monthly fossil fuel CO_2 emissions at 0.1°× 0.1° resolution, derived from internationally reported energy statistics and sector-specific activity data. The dataset integrates CO_2 emissions from fossil fuel combustion harmonized with IEA energy balances and includes detailed sectoral sources such as power generation, industrial processes, and transportation.

(4) CAMS Global Anthropogenic Emissions (CAMS-GLOB-ANT) version 6.2 (Soulie et al., 2024), developed within the Copernicus Atmosphere Monitoring Service (CAMS) framework, provides global monthly average anthropogenic CO_2 emissions at a spatial resolution of 0.1° × 0.1°. For CO2, Sectoral emissions are harmonized from EDGARv6.0 (Ferrario et al., 2021), CEDS (O'Rourke et al., 2021) and CAMS-GLOB-SHIP (Johansson et al., 2017) datasets, and the monthly temporal distribution is applied using profiles from CAMS-GLOB-TEMPO (Guevara et al., 2021).

https://doi.org/10.5194/egusphere-2026-2178
Preprint. Discussion started: 21 July 2026

(5) Global Carbon Budget Gridded Fossil Emissions Dataset (GCP-GridFED) version 2023.1 provides monthly fossil fuel CO_2 emissions globally at a resolution of 0.1° × 0.1° (Jones et al., 2021). These emissions are derived by scaling EDGAR v4.3.2 (2010) spatial patterns (Janssens-Maenhout et al., 2019) using national annual totals reported by the Global Carbon Budget (Friedlingstein et al., 2023), with spatial proxies such as population density and infrastructure distribution applied to ensure consistency with country-level emissions. For Japan, the seasonality is based on the multi-year average from the Carbon Monitor dataset, excluding 2020 (Dou et al., 2022; Liu et al., 2020).

These emission inventories differ in terms of spatial resolution, sectoral classifications, data sources, and disaggregation methodologies. It is important to note that four of the inventories (ODIAC, EDGAR, CAMS and GCP) are based on disaggregation of national emissions, while MOSAIC is constructed using best available country and regional specific data (emission factors, activity and spatial data). All the inventories indicate monthly emissions. To maintain consistency and comparability, each inventory was incorporated into the WRF-Chem model as anthropogenic CO_2 flux inputs, with diurnal and weekly variations applied using scaling factors based on Sugawara et al. (2021).

2.4 Biogenic and Ocean fluxes

Biogenic CO_2 fluxes were represented using the offline Vegetation Photosynthesis and Respiration Model (VPRM), as described by Mahadevan et al. (2008). Hourly net ecosystem exchange (NEE) estimated by VPRM were downscaled to generate gridded biogenic fluxes for 2018 over Japan to reproduce daytime photosynthetic uptake and nighttime respiration (Fig. 2a). To check the NEE derived from VPRM in the GTA, we compared the simulated biogenic CO_2 flux with eddy covariance observations at four forest sites within the modelling domain from the JapanFlux2024 dataset (Ueyama et al., 2025). The VPRM reproduced the observed seasonal cycle patterns very well, though the VPRM tends to produce slightly smaller uptake at midday and smaller respiration at night than observations during the growing season (May–August).

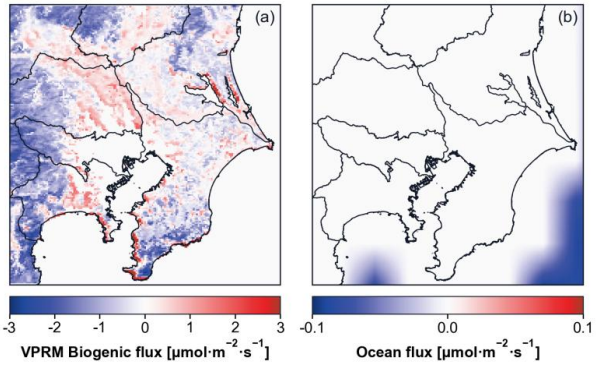

Figure 2: Spatial distributions of annual biogenic and ocean fluxes over the GTA.

Oceanic CO_2 fluxes were incorporated using the Carbon Dioxide Mapping Data (JMA Ocean CO_2 Map) developed by the Japan Meteorological Agency (Iida et al., 2021), which provides monthly air–sea CO_2 exchange based on observation–model synthesis (Fig. 2b). Both the biospheric and oceanic CO_2 fluxes are more than an order of magnitude smaller than the anthropogenic fluxes when integrated over the model domain. They are included to improve the representation of natural CO_2 variability and background concentrations over land and coastal regions.

https://doi.org/10.5194/egusphere-2026-2178
Preprint. Discussion started: 21 July 2026

2.5 Background CO_2 concentration, ΔCO_2, and fossil fuel CO_2

In order to compare observations with simulations with a focus on regional CO_2 enhancements (ΔCO_2) over the GTA, background CO_2 concentrations ($bgCO_2$) were defined using the MFJ data and the differences between the total CO_2 and the $bgCO_2$ concentrations (ΔCO_2) were discussed (in Sections 3.3-3.5). The observed CO_2 concentrations (CO_2^{obs}) at TST, YYG, NDA, and TKB were decomposed as:

$$CO_2^{obs}(t) = \Delta CO_2^{obs}(t) + bgCO_2^{MFJ,obs}(t) \quad (1)$$

where $bgCO_2^{MFJ,obs}$ represents the CO_2 concentration observed at MFJ, averaging within a ±5-day moving window (Figure 3). ΔCO_2^{obs} was defined as the differences between CO_2^{obs} and $bgCO_2^{MFJ,obs}$.

The simulated CO_2 concentration (CO_2^{sim}) was expressed as the sum of fossil fuel (anthropogenic) (CO_2^{ff}), biogenic (CO_2^{bio}), ocean (CO_2^{ocn}), and CAMS background (CO_2^{CAMS}):

$$CO_2^{sim}(t) = CO_2^{ff}(t) + CO_2^{bio}(t) + CO_2^{ocn}(t) + CO_2^{CAMS}(t) \quad (2)$$

and we expressed the ΔCO_2^{sim} as same manner as the observations:

$$CO_2^{sim}(t) = \Delta CO_2^{sim}(t) + bgCO_2^{MFJ,sim}(t) \quad (3)$$

where $bgCO_2^{MFJ,sim}$ represents the simulated CO_2 concentrations at the MFJ site. The fossil fuel, biogenic, and ocean components were found to be negligible at the altitude of the MFJ, resulting in the $bgCO_2^{MFJ,sim}$ being equivalent to the CAMS background field.

Figure 3 shows time series of $bgCO_2^{MFJ,obs}$ and $bgCO_2^{MFJ,sim}$ in 2018. The $bgCO_2^{MFJ,sim}$ was averaged between 22:00 and 23:00 JST to construct daily values and applied the same central ±5-day moving mean as $bgCO_2^{MFJ,obs}$. The observed and simulated CO_2 at MFJ have very similar seasonal cycle and day-to-day variability throughout 2018. The annual mean bias (simulation minus observation) was 0.2 ppm, and the maximum absolute difference is 3.3 ppm. The results demonstrated that the background CO_2 field used in our WRF-Chem CO_2 simulations was realistic and proper reference for the GTA. Figure 3 also illustrates the CAMS background CO_2 (CO_2^{CAMS}) at the four observation sites. An enhancement of background CO_2 were found at the four observation sites than at MFJ. Therefore, the difference between ΔCO_2^{obs} and ΔCO_2^{sim} based on the MFJ background level indicates a model-observation bias, stemming from both the WRF-Chem simulation and the CAMS background field in the GTA.

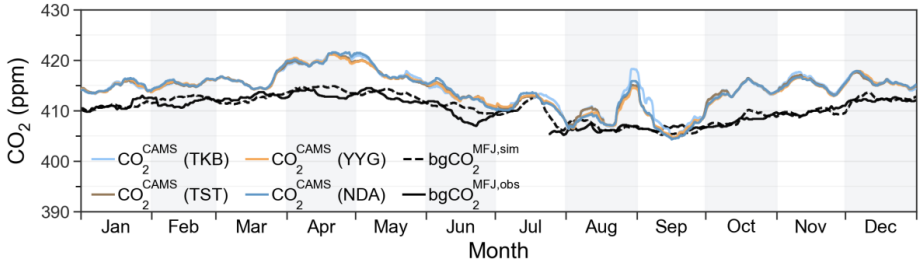

Figure 3: Time series of observed CO_2 at MFJ ($bgCO_2^{MFJ,obs}$), simulated CO_2 at MFJ ($bgCO_2^{MFJ,sim}$), and the CAMS background CO_2 (CO_2^{CAMS}) at the four observation sites (TKB, TST, YYG, and NDA) in 2018. Data gaps in $bgCO_2^{MFJ,obs}$ are due to missing observations.

https://doi.org/10.5194/egusphere-2026-2178
Preprint. Discussion started: 21 July 2026

Then, the simulated fossil fuel CO_2 ($FFCO_2^{sim}$, equal to CO_2^{ff}) was assessed using observations (Sections 3.6-3.7). We defined observed anthropogenic CO_2 ($FFCO_2^{obs}$) by removing the simulated biogenic, oceanic, and background components from CO_2^{obs}:

$$FFCO_2^{obs}(t) = CO_2^{obs}(t) - (CO_2^{bio}(t) + CO_2^{ocn}(t) + CO_2^{CAMS}(t)) \quad (4)$$

The accuracy of $FFCO_2^{obs}$ is influenced by the associated uncertainties in CO_2^{bio}, CO_2^{ocn} and CO_2^{CAMS}. Uncertainty in CO_2^{CAMS} would be small due to the substantial agreement between $bgCO_2^{MFJ,obs}$ and $bgCO_2^{MFJ,sim}$. $FFCO_2^{obs}$ was compared with the simulated CO_2^{ff} to evaluate the anthropogenic emission inventories. This approach is similar to previous studies, in which simulated non-fossil contributions were subtracted from observations to isolate the CO_2 enhancements due to anthropogenic emissions (Janardanan et al., 2016).

3 Results and discussion

3.1 Meteorological field

To evaluate the reliability of the meteorological fields used in the CO_2 transport simulations, we compared simulated wind fields with hourly Automated Meteorological Data Acquisition System (AMeDAS) observations from the Japan Meteorological Agency (https://www.data.jma.go.jp/obd/stats/etrn/index.php, accessed on 30 April 2025). The comparison focused on near-surface wind speed and wind direction at three representative stations located near the CO_2 observation sites: Tsukuba, Tokyo, and Miura. The simulated winds were interpolated to each station location, and standard statistical metrics were computed, including the mean bias (MB), root mean square error (RMSE), and Pearson correlation coefficient (r). For verification of simulated winds at the TST height, we used wind speed and direction measured from three azimuthal positions around the tower at approximately 200 m and 285 m altitudes. To compare, both observed and simulated winds were linearly interpolated to around 250 m. Then, the directional component associated with the highest wind speed at around 250 m was selected to represent the prevailing flow. The interpolated WRF-Chem outputs were then directly compared with the processed observations.

Comparison of wind speed and wind direction between the simulations and the observations showed that the model could generally reproduce the temporal variations in the wind fields and provided reasonable meteorological conditions for driving the transport of CO_2. The statistics summarized in Table 3 indicate that the simulated wind speeds were slightly higher than the observations. These results are consistent with Ohyama et al. (2023).

Table 3: Mean bias (MB), root mean square error (RMSE), and correlation coefficient (r) between the WRF-Chem simulations and observations.

Site	Metrological Station	Wind speed(m/s)			Wind direction (degree)		
		MB	RMSE	r	MB	RMSE	r
TKB	Tsukuba*	0.03	0.9	0.82	32.8	48.7	0.73
TST	Tokyo Skytree	1.9	3.2	0.79	-4.9	55.1	0.46
YYG	Tokyo*	0.9	1.7	0.74	31.0	45.7	0.72
NDA	Miura*	0.6	1.5	0.86	23.5	37.9	0.82

**AMeDAS station.*

https://doi.org/10.5194/egusphere-2026-2178
Preprint. Discussion started: 21 July 2026

3.2 Five emission inventories for GTA and the spatial distribution

To assess the spatial consistency among the anthropogenic CO_2 inventories, we compared the annual mean flux distributions from MOSAIC, ODIAC, EDGAR, CAMS-GLOB-ANT, and GridFED over the Kanto region (Fig. 4). All inventories consistently reproduce the highest CO_2 emissions over the Tokyo Bay area, where major industrial and power generation sources are concentrated. Emissions gradually weaken toward the surrounding urban and suburban regions, forming a decreasing gradient away from the bay. However, the spatial gradients and emission magnitudes differ considerably among datasets. The annual total anthropogenic CO_2 emissions (TgC yr^{-1}) were 78.7 for MOSAIC, 76.0 for ODIAC, 69.4 for EDGAR, 86.3 for CAMS-GLOB-ANT, and 85.0 for GridFED over the inner domain (d02).

The comparison between MOSAIC and ODIAC (Fig. 4f) shows that their overall emission patterns are similar, however, notable local contrasts exist across the GTA. ODIAC exhibits higher emissions than MOSAIC over the central and northwestern parts of Tokyo, reflecting its stronger weighting toward brightly illuminated commercial and industrial districts derived from nightlight data. In contrast, MOSAIC showed higher fluxes along the industrial corridor surrounding Tokyo Bay and in some suburban zones, influenced by detailed sectoral energy statistics used in its spatial allocation. Overall, ODIAC concentrates emissions more sharply in the urban core, whereas MOSAIC distributes them more broadly across surrounding industrial and residential regions.

The global inventories EDGAR, CAMS-GLOB-ANT, and GridFED have a lower spatial resolution (0.1°× 0.1°) compared with MOSAIC and ODIAC. This difference leads to smoother spatial patterns, as localized emission hotspots such as power plants around Tokyo Bay are spatially averaged into broader regions of enhanced flux. Consequently, their emission fields appear more continuous and less variable at the suburban scale. CAMS and GridFED, in particular, showed spatial differences from the other inventories along the eastern coast of Tokyo Bay and the Pacific shoreline.

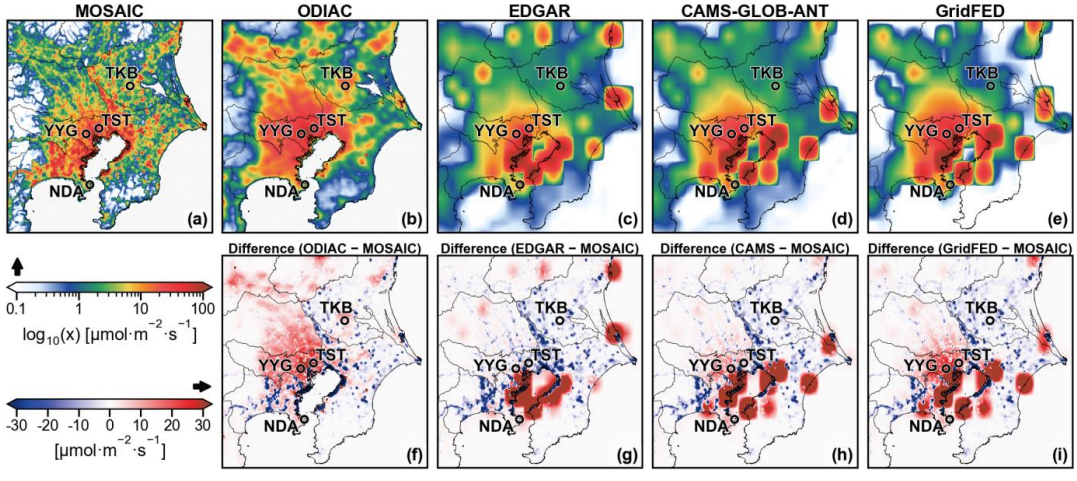

Figure 4: Anthropogenic CO_2 emission fluxes from five inventories in 2018 (top) and their differences relative to MOSAIC (bottom). Red indicates regions where the corresponding inventory shows higher emissions than MOSAIC, while blue indicates lower emissions. All datasets are regridded to the WRF domain for consistent comparison.

https://doi.org/10.5194/egusphere-2026-2178
Preprint. Discussion started: 21 July 2026

3.3 Time series of ΔCO_2

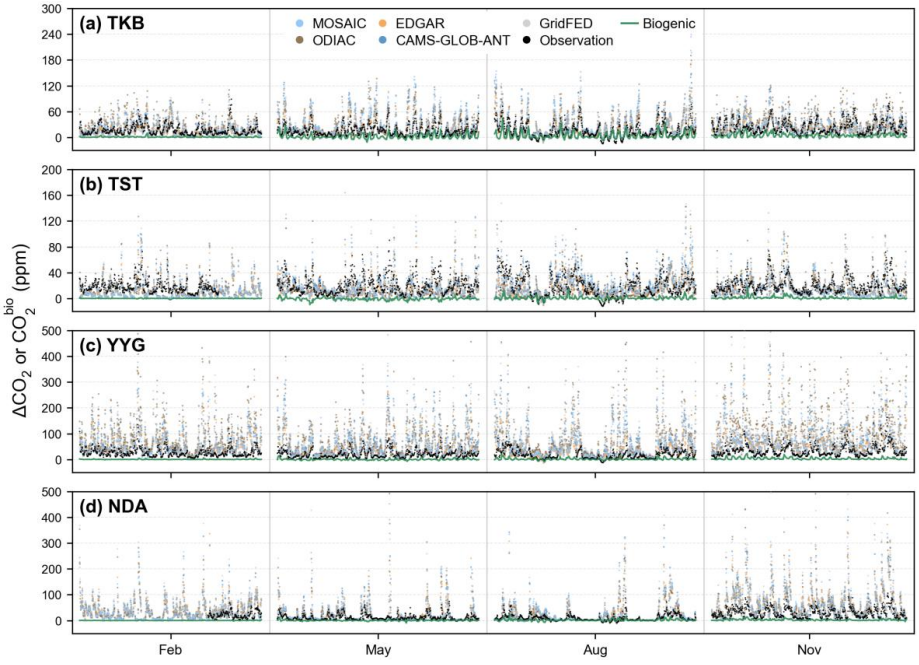

Figure 5: Simulated and observed hourly ΔCO_2 at TKB, TST, YYG, and NDA for four selected months in 2018 (February, May, August, and November). Black dots denote hourly observations; coloured dots show WRF-Chem simulations using five anthropogenic inventories, and the green line represents the hourly biogenic concentrations simulated by VPRM. Data gaps are due to missing observations.

Figure 5 compares hourly ΔCO_2 with WRF-Chem simulations driven by five anthropogenic inventories at four sites. To improve the visual clarity of the comparison among inventories, only four representative months (February, May, August, and November) are shown in Fig. 5, although the analysis was conducted for the full year of 2018. Across all sites, the simulations reproduced the synoptic scale variability and many rapid enhancements of ΔCO_2, while the amplitudes of these enhancements varied by inventories and by sites.

Among the four sites, TKB showed good agreement in both temporal variability and peak magnitudes. At TST, the simulated magnitudes are generally similar to the observations, although some differences may be related to errors in vertical mixing or transport at the tower height. At YYG, the simulated CO_2 captured the observed CO_2 enhancement patterns, but it overestimates several peaks by more than 200 ppm. At NDA, the model occasionally overestimates short peaks, but it reproduced extended low-concentration periods, and the overall variability is more consistent with the observations than YYG.

The ΔCO_2 included not only CO_2 enhancements emitted from anthropogenic sources but also CO_2 variations due to source and sink by biosphere and ocean. Fig. 5 also illustrates CO_2^{bio}. The diurnal variations of CO_2^{bio} were seen at TKB from spring to fall, while CO_2^{bio} concentrations and variations were very small at other sites. The magnitude of CO_2^{bio} variations was significantly smaller than the large enhancement of ΔCO_2 even at TKB. Annual averaged CO_2^{bio} source (mean of positive values) and sink (mean of negative values) were 4.4±4.8 ppm and –1.5±1.5 ppm at TKB, 1.1±1.5 ppm and –1.0±1.1 ppm at TST, 2.5±3.1 ppm and –1.1±1.1 ppm at YYG, and 1.9±2.6 ppm and –0.9±1.1 ppm at NDA, respectively. The CO_2^{ocn} sink was almost zero. Thus, the most of ΔCO_2 variations, especially for large enhancements, were caused by anthropogenic CO_2 emissions in the GTA.

Inventory-dependent differences are expressed mainly in peak amplitudes rather than event timing. The spatial contrasts among the emission inventories (Fig. 4) help explain the site-dependent variations shown in Fig. 5. Inventories that assign stronger

https://doi.org/10.5194/egusphere-2026-2178
Preprint. Discussion started: 21 July 2026

emissions to the Tokyo Bay industrial area (e.g., CAMS-GLOB-ANT and GridFED) and the central urban area (e.g., ODIAC) produce higher simulated ΔCO_2 peaks at the urban site YYG, whereas those with more diffuse spatial distributions or lower total emissions (e.g., MOSAIC and EDGAR) generate weaker short-term ΔCO_2 peaks. These differences interact with the seasonal boundary-layer structure and monsoonal circulation over Tokyo: during the winter monsoon (characterized by prevailing northwesterlies and a shallow PBL), CO_2 emitted from the metropolitan core tends to accumulate and be advected southeastward, enhancing the high-concentration events at YYG and intermittently affecting NDA when the flow aligns with the Tokyo Bay. In contrast, during summer, south winds bring in low-CO_2 air from the Pacific Ocean, thereby suppressing CO_2 peaks at the southern sites, particularly at NDA. This monsoon-influenced behaviour indicates that the timing of enhancement events is primarily governed by synoptic and boundary-layer dynamics, while the amplitude depends on the spatial distribution and magnitude of emissions as well as the efficiency of transport at different heights.

3.4 Influence of the emission mapping and wind direction on ΔCO_2

We examined directional dependence of ΔCO_2 to assess how different emission inventories represent spatial emission patterns. Figure 6 presents the ΔCO_2 averaged within wind direction and wind speed sectors from 0 to 20 m s^{-1} (upper panels) and the directional distribution of the inventory fluxes around each site with distance from 0 to 50 km (lower panels). They provide observation-based atmospheric signatures of upwind emission source regions at each station, enabling a direct evaluation of whether the model reproduces the observed directional structure and how strongly the simulated enhancements respond to differences in inventory spatial allocation. The enhanced ΔCO_2 air masses were observed and simulated in the directions connecting with high CO_2 emission area in the central Tokyo and the Tokyo Bay industrial area and the magnitude of these direction-averaged values varied among inventories. The interpretation of these directional signals also needs to consider the seasonal wind pattern around Tokyo Bay, where north–south flow predominates, with southerly winds occurring most frequently in summer and northern winds being more dominant in winter. This seasonality likely modulates the relative influence of the Tokyo Bay and inland source regions on observed ΔCO_2.

At the suburban TKB, the five inventories showed similar directional patterns but different magnitudes. Observations indicated the largest ΔCO_2 under south-westerly winds, which corresponded to transport from the Tokyo metropolitan area. The simulations reproduced ΔCO_2 increases in this direction, although the strength differs among inventories. MOSAIC and ODIAC showed higher ΔCO_2 because they assigned stronger emissions around the northern Tokyo suburban and industrial areas rather than other inventories with coarser spatial patterns. EDGAR showed more moderate ΔCO_2 and a smoother spatial imprint, indicating weaker localized hotspots around the near field suburban industrial areas. MOSAIC and ODIAC showed higher fluxes in the southwest to south sectors within the inner 10–30 km rings, matching the upwind direction of the observed enhancement. The observed and simulated ΔCO_2 increases at TKB were mainly influenced by air flow from the Tokyo Bay area and nearby urban regions.

At TST, high tower in the central Tokyo, both the observations and simulations showed enhanced ΔCO_2 under south-southwesterly flow with higher wind speeds, which corresponds to the large emissions from industrial and power-plant zone along the west side and east side of Tokyo Bay, respectively. The Tokyo Bay area frequently influenced the CO_2 concentrations at TST, consistent with Yamada et al. (2025). Among the inventories, the observed south-southwest enhancement of ΔCO_2 was less represented in ODIAC, because the ODIAC emissions along the west side of the Tokyo Bay were weaker than those in other inventories. EDGAR captured the Tokyo Bay influence with intermediate strength, but with reduced directional contrast compared to inventories that resolve sharper coastal and industrial gradients. This reduced contrast indicates that smoother spatial allocation can mute the distinct Tokyo Bay signature in the atmospheric response, whereas inventories with finer coastal/industrial gradients tend to preserve stronger sector-to-sector differences that are more consistent with the

https://doi.org/10.5194/egusphere-2026-2178
Preprint. Discussion started: 21 July 2026

observed directional enhancement. Although north-westerly winds dominated in winter, their influence on ΔCO_2 was weaker. The upwind area in the north of TST contains mainly residential and transportation sources with lower emission intensity, and the higher wind speeds during these periods would dilute the high ΔCO_2 spikes.

At the urban core site YYG, the observed ΔCO_2 distribution indicated that the main influences occurred under north-westerly and south-easterly winds. This pattern reflects the combined impacts of transport from central Tokyo and Tokyo Bay. However, the simulated ΔCO_2 was high in almost all directions and ODIAC and GridFED producing the largest values. This might be caused from broadly high-level fluxes surrounding YYG, with the strongest values concentrated within 0–20 km across all directions. The higher ODIAC values might be explained by its spatial distribution, which placed more emissions in the densely built-up residential areas surrounding YYG and therefore increased flux contributions in several directions. In comparison, EDGAR produced lower and smoother direction-averaged ΔCO_2 than others, suggesting weaker urban core flux intensity and a more diffuse spatial allocation around YYG. Slightly lower values toward the west corresponded to relatively weaker emissions in that sector across the inventories. The models reproduced the correct dominant sectors but overestimate the amplitude of direction-averaged ΔCO_2, indicating that urban-core fluxes were likely too strong relative to observations.

At the coastal site (NDA), observed CO_2 enhancements were associated with northerly winds, with the largest concentrations linked to the Tokyo Bay sector. The simulations reproduced this pattern, indicating that most high-concentration events at NDA were driven primarily by this atmospheric transport rather than by local emissions. However, all inventories showed an overall positive bias in the northern enhancement. Among them, EDGAR, CAMS-GLOB-ANT and GridFED showed particularly large values because their emissions along the western Tokyo Bay coast were stronger than the other inventories, whereas ODIAC agreed more closely with the observed levels. The corresponding flux maps highlighted a pronounced high-flux corridor in the inland-to-bay sectors consistent with the wind directions that produce elevated ΔCO_2 at NDA. NDA therefore provides an observational constraint on the spatial distribution of emissions around Tokyo Bay, as the observed ΔCO_2 enhancements clearly reflect how emissions are allocated in this coastal sector by different inventories.

The differences between the YYG and TST sites are likely influenced by vertical boundary-layer processes rather than horizontal emission distribution alone. At YYG, the higher simulated ΔCO_2 probably reflect the accumulation of emissions within the stable or shallow boundary layer over high-emission areas. At TST, the situation is different: because of its high measurement altitude, the observations integrate air masses influenced by a broader regional footprint. As a result, the simulated ΔCO_2 at TST agrees well with the observations, showing only small biases.

Overall, the direction-averaged ΔCO_2 patterns derived from observations and simulations at the four sites captured the correct upwind directions linking to the Tokyo metropolitan core and the Tokyo Bay industrial area. The consistent dominant wind sectors between observations and simulations indicated that the spatial allocation of emissions in the inventories is broadly consistent with the real emission distribution. At the same time, the observation based directional signatures provide a practical atmospheric basis to characterize and distinguish inventories, including those with similar distribution patterns (e.g., EDGAR, CAMS-GLOB-ANT, and GridFED), because they can differ in directional contrast and in how distinctly they capture the Tokyo Bay signal. Differences in simulated amplitude mainly arose from how each inventory distributed and scaled emissions. High-resolution datasets such as MOSAIC and ODIAC assigned stronger fluxes to the urban center and nearby suburban–industrial areas, giving larger directional contrasts at downwind sites. In contrast, CAMS-GLOB-ANT and GridFED allocated stronger emissions along the Tokyo Bay coast, leading to higher simulated concentrations in the coastal and downwind sectors. EDGAR showed smoother flux patterns and medium ΔCO_2, resulting in weaker directional gradients than MOSAIC/ODIAC while still captured theΔCO_2 from dominant upwind sectors. The observations further support the benefit of fine emission representation: inventories that resolve sharper coastal and industrial gradients tend to reproduce clearer Tokyo Bay–related directional contrasts, whereas smoother spatial allocation can mute these contrasts by spreading emissions more diffusely across sectors and distances. These results indicate that the spatial pattern of anthropogenic emissions governs the directional gradients, while emission intensity, atmospheric transport, and boundary-layer mixing together control their overall magnitude.

https://doi.org/10.5194/egusphere-2026-2178
Preprint. Discussion started: 21 July 2026

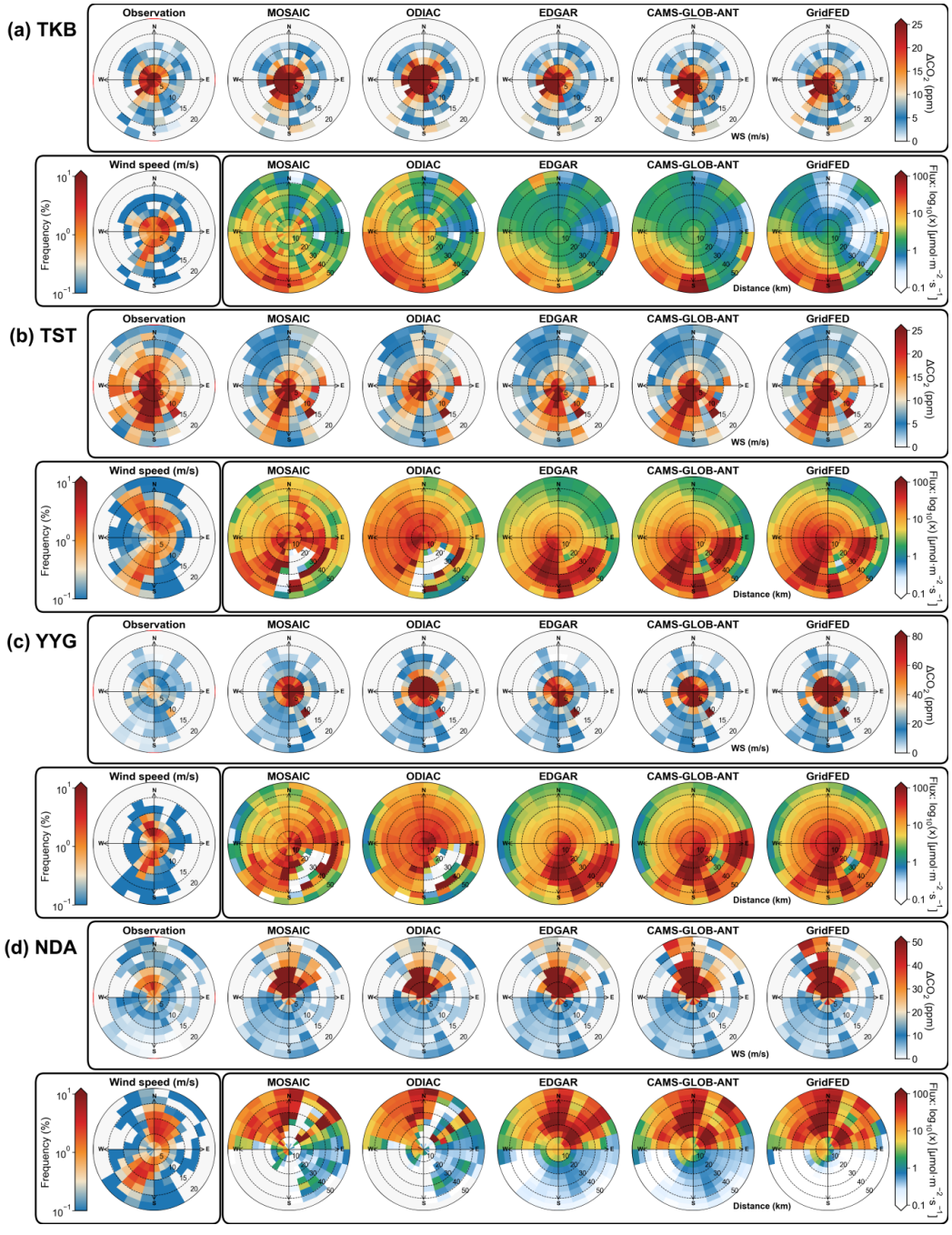

Figure 6: Wind-sector–averaged ΔCO_2 at four stations. Top: observed and simulated ΔCO_2 concentration. Bottom-left: frequency of wind speed and wind direction. Bottom-right: CO_2 fluxes from each inventory, averaged in distance–direction bins around the station (radial distance: 0–50 km).

https://doi.org/10.5194/egusphere-2026-2178
Preprint. Discussion started: 21 July 2026

3.5 Diurnal cycles of ΔCO_2

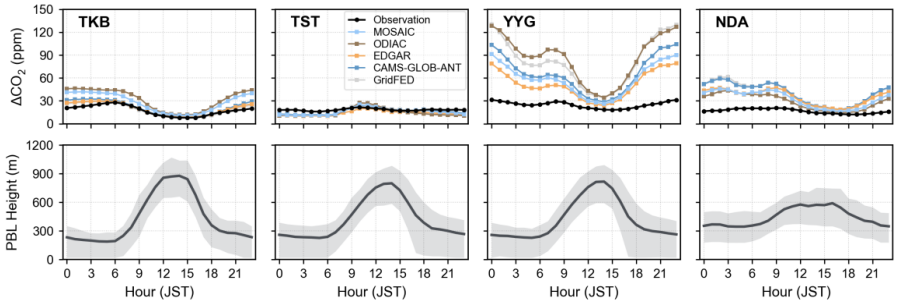

Figure 7: Diurnal cycles of ΔCO_2 and planetary boundary layer height (PBLH) in Japan Standard Time. Top panels show simulated ΔCO_2 from five emission inventories and observations. Bottom panels show simulated PBLH (mean and interquartile range).

Figure 7 shows the mean diurnal cycles of ΔCO_2 and planetary boundary layer height (PBLH) at the four sites in summer (June–August) and winter (January–February and December) for the five emission inventories and the observations. Except TST, ΔCO_2 was high in the early morning, reached its lowest value around noon, and increased again in the evening, whereas PBLH was shallow at night, grew rapidly after sunrise, and reached a maximum between about 12:00 and 15:00 JST. This opposite pattern between ΔCO_2 and PBLH is consistent with basic boundary layer processes: at night a shallow, stable layer keeps local emissions close to the surface, while during the day a deeper, well-mixed layer spreads and dilutes them. The timing of the diurnal changes of ΔCO_2 was similar at all four sites, but the amplitude of the daily change was different. The suburban site TKB had the small day–night range, whereas the urban core site YYG had the largest range. At the tower site TST, the diurnal cycle was much weaker than the other sites, which is consistent with smaller direct impact from surface emissions at that level. At the coastal site NDA, ΔCO_2 showed clear early-morning and evening enhancements, while values around local noon were relatively low. A clear seasonal contrast was also evident: PBLH was generally deeper in summer and remained elevated for a longer period from noon to afternoon, whereas in winter it showed a narrower midday peak. Correspondingly, morning and evening ΔCO2 enhancements were generally stronger in winter, especially at YYG and NDA. Differences among inventories appeared mainly in the amplitude of the diurnal cycle rather than in its timing. Inventories that assigned relatively large total emissions to the central area and Tokyo Bay area (ODIAC, GridFED, and CAMS-GLOB-ANT) produced stronger early morning and evening ΔCO_2 peaks, especially at YYG. In contrast, inventories with lower or more spatially diffuse urban emissions (EDGAR and MOSAIC) yielded smaller peaks and were often closer to the observations around noon, when the PBL was deepest and mixing was most effective. The irregular ΔCO_2 enhancement between about 06:00 and 09:00 JST can be explained by the combination of the shallow morning PBL and the diurnal scaling factors applied to the inventories. In our simulations, hourly emissions are obtained by multiplying the monthly mean fluxes by diurnal factors that peak during the morning and evening rush hours for the traffic sector.

The results demonstrated that the combination of diurnal emission factors and PBL evolution explained the observed structure of the ΔCO_2 diurnal cycle, and that differences among inventories were expressed mainly through the amplitude of ΔCO_2 enhancement in the PBL in the densely urbanized areas. Many urban CO_2 studies focused on daytime or afternoon data, when the boundary layer was deep and better represented in models, to reduce transport errors in emission inversions. Large mismatches between simulation and observation are more common at night because stable boundary layers and shallow mixing are complex to simulate (Brunner et al., 2019; McKain et al., 2012). Therefore, we evaluated anthropogenic inventories on the midday period (12:00–15:00 JST), when the boundary layer is relatively deep and better represented in mesoscale models, and previous urban CO_2 studies have shown that this window is more suitable for estimating emissions (Lian et al., 2022, 2024; Martin et al., 2019).

https://doi.org/10.5194/egusphere-2026-2178
Preprint. Discussion started: 21 July 2026

3.6 Comparison of $FFCO_2$ among inventories

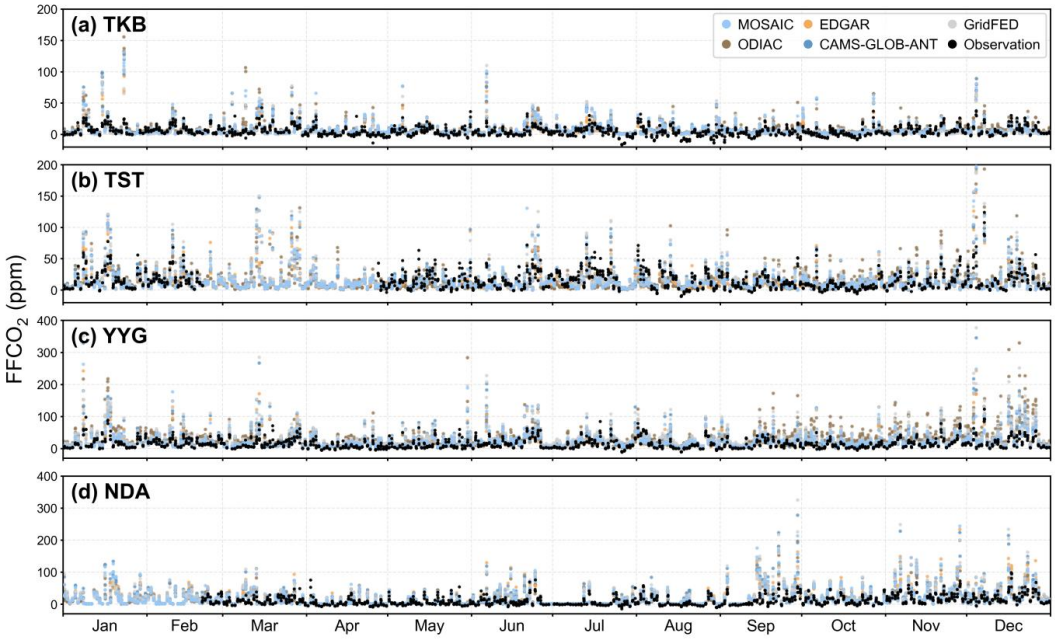

Figure 8: Simulated and observed $FFCO_2$ between 12:00 and 15:00 JST at four sites in 2018. Data gaps are due to missing observations.

To evaluate the anthropogenic emission inventories, we compared $FFCO_2^{obs}$ and $FFCO_2^{sim}$ for midday between 12:00 and 15:00 JST (Fig. 8). At TKB and TST, the simulated $FFCO_2$ agreed well with the observations; differences among inventories were usually small and the day-to-day variability was also reproduced well. At YYG, strong enhancements occurred more often and the contrast among inventories was clearer: ODIAC and GridFED generally provided the highest values, and EDGAR and MOSAIC were often closer to the observed peaks, as with the same reasons discussed in Section 3.4. At NDA, the simulations captured the midday baseline and variability for most days, except for a few high $FFCO_2$ events where all inventories showed larger enhancements than the observation. Overall, the midday time series indicated that the simulation reproduced $FFCO_2$ reasonably well and that differences in the spatial distribution and total strength of emissions among inventories mainly controlled the magnitude and frequency of high $FFCO_2$ events.

https://doi.org/10.5194/egusphere-2026-2178
Preprint. Discussion started: 21 July 2026

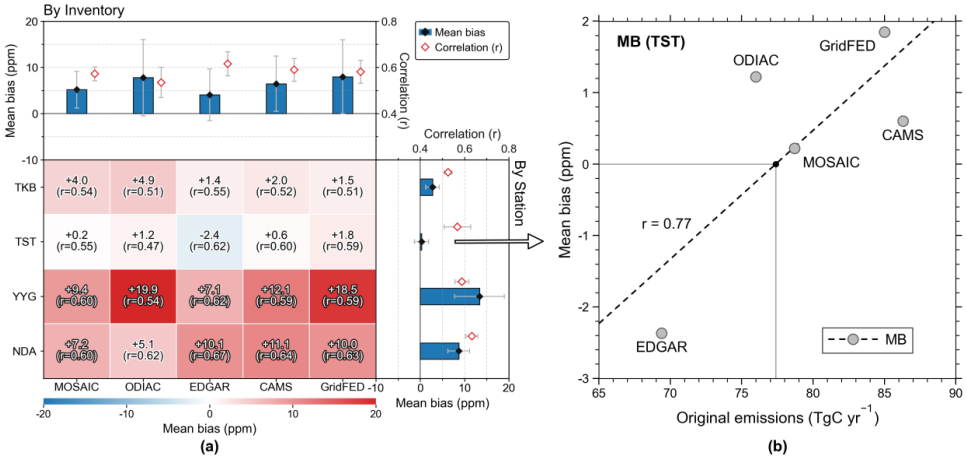

Figure 9: (a) Performance of simulated $FFCO_2$ using five anthropogenic emission inventories against observations at four sites during 12:00–15:00 JST. Mean bias (MB, ppm) and correlation (r) are summarized by inventory and station. (b) Relationship between MB at TST and the original annual CO_2 emission totals across the five inventories. The dashed line shows the linear fit, and the black point indicates the emission value at MB = 0.

Figure 9 (a) shows the MB and r between $FFCO_2^{obs}$ and $FFCO_2^{sim}$ during the midday period (12:00–15:00 JST) and summarize the results by site and by inventory. By station, TKB showed a modest positive MB for all inventories (1.4 to 4.9 ppm), indicating generally good agreement between the simulations and observations. TST exhibited the smallest bias (−2.4 to 1.8 ppm), suggesting the best agreement in concentration magnitude among four sites. YYG showed the largest positive MB for all inventories (7.1–19.9 ppm). NDA showed a positive MB (5.1–11.1 ppm) but the highest correlation (r = 0.60–0.67) among the four sites, suggesting that temporal variability was captured but concentrations were slightly overestimated.

Across inventories, clear differences in spatial allocation and emission strength are evident (Fig. 4). EDGAR provided the smallest overall MB (4.2 ppm) and the highest correlation (r = 0.63). This is mainly because EDGAR showed lower positive biases at YYG and NDA than the other inventories, resulting in smaller deviations. ODIAC produced the largest positive MB at YYG (19.9 ppm), as it assigned very strong fluxes to the urban core, where dense population and nightlight proxies dominated its distribution. The horizontal distribution of MOSAIC emissions was similar to ODIAC but produced smaller bias at YYG (9.4 ppm), reflecting lower flux in central Tokyo. However, MOSAIC showed a higher MB than ODIAC at NDA, consistent with its stronger flux allocation along the southwestern Tokyo Bay coast. CAMS-GLOB-ANT and GridFED maintained moderate correlations at most sites, but both overestimated at the urban (YYG) and coastal (NDA) area. This agrees with their enhanced fluxes along western Tokyo Bay, where power plants are concentrated.

Overall, the inventory follows the expected effect of spatial allocation and resolution. Inventories that place more emissions in the urban core and bay area generate higher concentrations. The overall amplitude depends mainly on where and how strongly emissions are distributed. The systematic overestimation across inventories is largely driven by YYG, where urban emissions are most concentrated. EDGAR's better performance likely arises from its lower total flux. In contrast, MOSAIC, despite having total emissions comparable to ODIAC, CAMS, and GridFED, showed the second-smallest bias, suggesting a more realistic spatial representation.

As a supplementary diagnostic, we examined the relationship between the MB values and the corresponding original CO_2 emission totals at TST across the five inventories. Because of its high observation height, TST likely represents a broader urban footprint and is less sensitive to local-scale spatial heterogeneity and short-term noise. Fig. 9 (b) shows that MB tends to increase with increasing original emission total across the five inventories. The analysis showed a positive relationship (r = 0.77), and linear interpolation to MB = 0 gave an indicative value of about 77.4 Tg C yr^{-1}. Although this approach cannot capture the influence of spatial distribution on MB, it is still useful for estimating the total emission magnitude of the GTA.

https://doi.org/10.5194/egusphere-2026-2178
Preprint. Discussion started: 21 July 2026

3.7 Emission comparison and implications

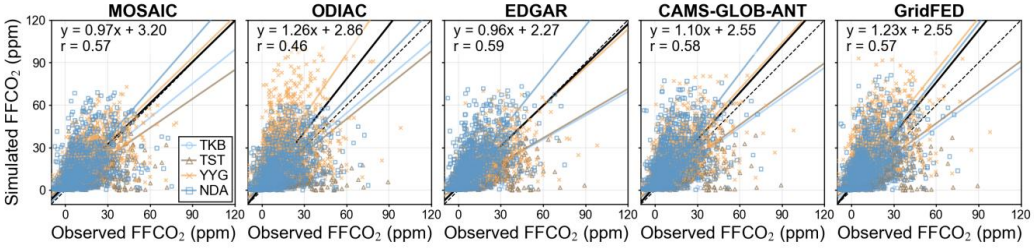

Figure 10: Relationship between simulated and observed midday $FFCO_2$ (12:00–15:00 JST) for five emission inventories, combining data from all four sites. Coloured bins show two-dimensional histograms after removing values outside ±2σ. The dashed line indicates the 1:1 line, and the red line shows the reduced major axis regression.

Figure 10 shows the relationship between simulated and observed $FFCO_2$ for the five emission inventories, integrating data from all four sites and using only the midday values. Data outside ±2σ of the total mean at each station were removed to exclude extreme events. Reduced major axis (RMA) regression was applied because both $FFCO_2^{obs}$ and $FFCO_2^{sim}$ contain random errors. The slopes between $FFCO_2^{obs}$ and $FFCO_2^{sim}$ differed among inventories. MOSAIC and EDGAR have slopes close to 1.0, indicating that the simulations reproduce the amplitude of observed midday variations reasonably well. CAMS-GLOB-ANT and GridFED showed slopes above 1, suggesting that they overestimated the observed enhancements. ODIAC exhibits the largest slope, because the regression using data combined across all four sites is strongly affected by the YYG site. YYG often showed the most apparent $FFCO_2$ enhancements, and more importantly, the largest departure from the 1:1 relationship between simulated and observed $FFCO_2$, which pulls the fitted slope and correlation when all stations are analysed together. This influence is present for all inventories in the four-site analysis, but it is most apparent for ODIAC because ODIAC allocates higher emissions in the vicinity of YYG, leading to larger simulated $FFCO_2$ enhancements at YYG than at the other sites. Overall, the inventories capture much of the temporal variability, but notable scatter remains.

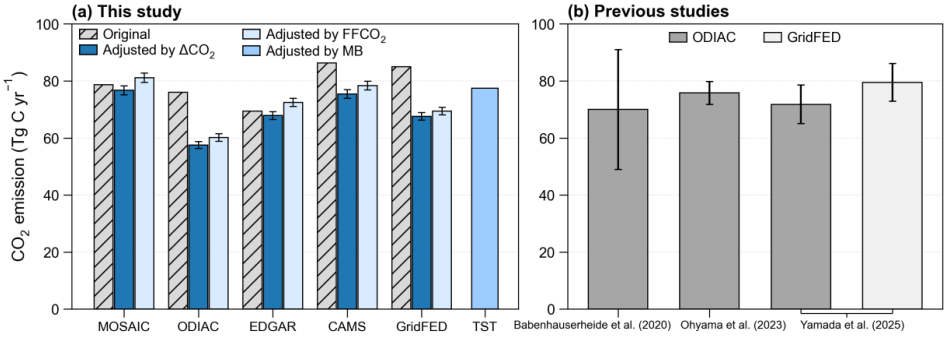

Figure 11: Comparison of anthropogenic emissions over the GTA. (a) This study: original inventory totals (hatched bars) and adjusted values (blue bars) using scaling factors derived from the midday (12:00–15:00 JST) RMA slopes at all four sites, and the TST estimate adjusted by MB. Error bars represent ±1σ uncertainty. (b) Previous studies: top-down estimates based on ODIAC or GridFED (Babenhauserheide et al., 2020; Ohyama et al., 2023; Yamada et al., 2025).

We then use the RMA slopes (Fig. 10) as scaling factors to adjust the annual total emissions from each inventory. Figure 11a compares the original and adjusted emissions for the five inventories, together with the TST-based estimate of 77.4 Tg C yr^{-1} (Section 3.6). The primary scaling is based on $FFCO_2$, but we also apply the same scaling approach to ΔCO_2 as a simple robustness check, because ΔCO_2 includes biogenic (and ocean) contributions and therefore provides uncertainties arisen from biospheric flux. The $FFCO_2$ and ΔCO_2 based adjustments are similar (Fig. 11a), indicating that the biogenic and ocean

https://doi.org/10.5194/egusphere-2026-2178
Preprint. Discussion started: 21 July 2026

contributions are small and have little impact on the inferred scaling. Using the $FFCO_2$-based scaling, the adjusted emissions are 81.1 ± 1.6 Tg C yr^{-1} for MOSAIC, 60.2 ± 1.3 Tg C yr^{-1} for ODIAC, 72.5 ± 1.4 Tg C yr^{-1} for EDGAR, 78.4 ± 1.5 Tg C yr^{-1} for CAMS-GLOB-ANT, and 69.4 ± 1.3 Tg C yr^{-1} for GridFED. The MOSAIC and EDGAR inventories are most consistent with the measurements and change very little after adjustment. The ODIAC, CAMS-GLOB-ANT, and GridFED inventories are corrected downward largely.

For comparison, Fig. 11b illustrates previous top-down studies for the GTA: reported total fossil-fuel CO_2 fluxes of 71.8 ± 6.8 Tg C yr^{-1} and 79.5 ± 6.6 Tg C yr^{-1} using ODIAC and GridFED separately with TST-based regression (Yamada et al., 2025), 75.8 ± 4.0 Tg C yr^{-1} based on ground-based FTIR column measurements (Ohyama et al., 2023), and 70 ± 21 Tg C yr^{-1} based on TCCON and radiosonde profiles (Babenhauserheide et al., 2020). These studies use different model domains, time periods, and observation types, and they rely on different observing systems and transport models (global or regional), so the absolute emissions cannot be compared one-to-one. However, they consistently point to a range of about 70–80 Tg C yr^{-1} for fossil-fuel CO_2 emissions around Tokyo. Our multi-site adjusted totals fall within or close to this range (and within the broader uncertainty ranges reported), which suggests that our estimate is broadly consistent with these independent constraints despite the different methods and domains. At the same time, this agreement should be interpreted as a consistency check rather than a strict one-to-one validation, because the underlying domains, periods, and observational constraints differ.

Although all these studies focus on the GTA, their spatial domains, observation periods, observation networks, and transport models are not the same, so the total emissions cannot be compared directly. Yamada et al. (2025) used the TST site and a global NICAM-based transport model (NICAM-TM), while our study uses the regional WRF-Chem model with nested high-resolution domains over GTA. These differences in model resolution and domain, together with the different site selections, can also lead to differences in the simulated ΔCO_2 fields. That study also pointed the insufficient representativeness of relying on a single site, and our multi-site results support the same conclusion. Even when we use the same ODIAC emission inventory, the simulated ΔCO_2 at each site on its own would suggest a different emission adjustment. This means that urban-scale emission estimates depend strongly on which sites are used and, on their location, height, and other characteristics. An observation network that includes both urban and suburban stations can reduce this site dependence and provide a more balanced constraint on fossil-fuel CO_2 emissions over the metropolitan areas.

Overall, these five bottom-up inventories tend to slightly overestimate the total emissions, whereas EDGAR and MOSAIC showed the best overall match to the original value. These results indicate that emission magnitude is as important as spatial allocation for reproducing observed CO_2 variability.

4 Conclusion

In this study, we used year-long high-resolution WRF-Chem simulations and continuous CO_2 observations from four sites to evaluate five anthropogenic CO_2 emission inventories (MOSAIC, ODIAC, EDGAR, CAMS-GLOB-ANT, and GridFED) over the Greater Tokyo Area (GTA). The simulations reproduced much of the observed ΔCO_2 and $FFCO_2$ variability. Elevated ΔCO_2 was associated with transport from the urban core and the Tokyo Bay, while the amplitudes differed among the five inventories. The four observation sites represent different GTA subregions and provide complementary constraints on inventory spatial patterns. In particular, YYG is most sensitive to emissions in the urban core, TKB provides a strong constraint on emissions in the northern suburban area, and NDA is especially useful for evaluating how emissions are distributed around Tokyo Bay. These results showed that multi-site observations are essential for urban emission assessment.

The analysis indicates that the main differences among inventories are related to spatial allocation and emission magnitude. Stronger northern suburban emissions in MOSAIC and ODIAC explain the higher simulated ΔCO_2 at TKB, whereas stronger nearby urban-core emissions in ODIAC and GridFED explain the higher ΔCO_2 at YYG. CAMS-GLOB-ANT and GridFED

https://doi.org/10.5194/egusphere-2026-2178
Preprint. Discussion started: 21 July 2026

tend to overestimate ΔCO_2 at NDA because of larger emissions along the Tokyo Bay coast. EDGAR showed the lowest overall bias, although its spatial distribution is coarser and more diffuse than those of MOSAIC and ODIAC. The correlation analysis between observed and simulated midday (12:00–15:00 JST) $FFCO_2$ showed the best consistency for EDGAR and MOSAIC and stronger overestimation for CAMS-GLOB-ANT, GridFED, and ODIAC (mainly driven by YYG). Applying the multi-site slopes as scaling factors, the adjusted GTA totals were 81.1 ± 1.6 (MOSAIC), 60.2 ± 1.3 (ODIAC), 72.5 ± 1.4 (EDGAR), 78.4 ± 1.5 (CAMS-GLOB-ANT), and 69.4 ± 1.3 Tg C yr^{-1} (GridFED). Meanwhile, the relationship between the mean bias at TST and the original CO_2 emission totals across the five inventories suggests a GTA emission estimate of 77.4 Tg C yr^{-1}.These values are broadly consistent with the ~70–80 Tg C yr^{-1} range reported by previous top-down studies for Tokyo, but this agreement should be interpreted as a consistency check because domains, periods, observing systems, definition of the background CO_2, and transport models differ.

These findings also highlight the importance and challenge of site selection in urban CO_2 studies, because different sites sample different subareas of the GTA and therefore provide different constraints on emissions. This means that evaluation based on a single site can lead to site-dependent conclusions. For further improvement of CO_2 emission inventories for the GTA, more work is needed on sectoral detail, spatial distribution, temporal distribution, and total emission magnitude. In particular, the spatial distribution should be improved in the urban core and along the Tokyo Bay coast, where the observations clearly distinguish differences among inventories. In addition, coarse inventories such as EDGAR may poorly represent large point sources, especially power plants. For urban-scale simulations, these emissions should be re-attributed to their exact locations to avoid large representation errors and to better reproduce localized enhancements. And a more realistic vertical allocation of emissions would also likely improve the accuracy of simulations. These conclusions should nevertheless be interpreted with some caution, because the summit of Mt. Fuji is the best available background reference in this study rather than a perfect one, and the observation-based $FFCO_2$ estimate still depends partly on simulated biogenic contributions. Overall, this study shows where inventories diverge within a megacity and provides a practical benchmark for improving urban CO_2 inventories and future urban emission monitoring.

Data availability

The observation data can be provided by the corresponding authors upon request. The MSM–GPV data were collected and distributed by Research Institute for Sustainable Humanosphere, Kyoto University (https://database.rish.kyoto-u.ac.jp/arch/jmadata/data/gpv/original/). The wind speed and wind direction data used in this study are publicly available from the "Past Meteorological Data Download" service of the Japan Meteorological Agency (JMA) at (https://www.data.jma.go.jp/gmd/risk/obsdl/index.php). The NCEP GDAS/FNL 0.25 Degree Global Tropospheric Analyses and Forecast Grids were obtained from the Research Data Archive at NCAR (https://rda.ucar.edu/datasets/d083003/#). The ERA5 reanalysis product can be retrieved from the Copernicus Climate Change Service Climate Data Store (https://cds.climate.copernicus.eu/cdsapp#!/dataset/reanalysis-era5-pressure-levels?tab=overview, last access: 25 July 2023).

Author contributions

YTe, TO and ZY designed the study. ZY performed the simulations and data analysis and prepared the manuscript with YTe. YTe performed the CO_2 observations and ensured data quality at MFJ, TST, YYG, NDA and TKB. TL and CA provided theoretical and technical support for the simulations. MN and HO optimized the meteorological fields for the simulations. MSai provided the MOSAIC data. SI and HS supported the observations at YYG and NDA. TM and MSas prepared the CO_2 scale used for observations. YTo supported the analysis and discussion. All authors contributed to the discussion and revisions of the manuscript.

https://doi.org/10.5194/egusphere-2026-2178
Preprint. Discussion started: 21 July 2026

Competing interests

The authors declare that they have no conflict of interest.

Acknowledgements

Wind data at TST were provided by TOBU TOWER SKYTREE Co., Ltd. The WRF-Chem simulations were performed using the supercomputer system of National Institute for Environmental Studies. The AW3D30 dataset was provided by the Japan Aerospace Exploration Agency. We also acknowledge the valuable support from Carla D'angeli, Ke Che, Alohotsy Rafalimanana and other colleagues at Reims Champagne-Ardenne, GSMA.

Financial support

This study was supported by the Environment Research and Technology Development Fund (JPMEERF24S12202) of the Environmental Restoration and Conservation Agency, provided by the Ministry of the Environment of Japan. TO is supported by NASA grant #80NSSC25K7212.

References

Abdallah, C., Lauvaux, T., Lian, J., Bréon, F.-M., Ramonet, M., Laurent, O., Ciais, P., Denier van der Gon, H. A. C., Dellaert, S., Perrussel, O., Baudic, A., Utard, H., and Gros, V.: A Gradient-Descent Optimization of CO_2–CO–NO_x Emissions over the Paris Megacity─The Case of the First SARS-CoV-2 Lockdown, Environ. Sci. Technol., 58, 302–314, https://doi.org/10.1021/acs.est.3c00566, 2024.

Ahn, D. Y., Goldberg, D. L., Coombes, T., Kleiman, G., and Anenberg, S. C.: CO_2 emissions from C40 cities: citywide emission inventories and comparisons with global gridded emission datasets, Environ. Res. Lett., 18, 034032, https://doi.org/10.1088/1748-9326/acbb91, 2023.

Alberti, R. C. A., Lauvaux, T., Vara-Vela, A. L., Barrero, R. S., Karoff, C., Andrade, M. D. F., Marques, M. T. A., Benavente, N. R., Cabral, O. M. R., da Rocha, H. R., and Ynoue, R. Y.: Monitoring and modeling seasonally varying anthropogenic and biogenic CO_2 over a large tropical metropolitan area, Atmospheric Chem. Phys., 25, 9803–9829, https://doi.org/10.5194/acp-25-9803-2025, 2025.

Arioli, M. S., D'Agosto, M. de A., Amaral, F. G., and Cybis, H. B. B.: The evolution of city-scale GHG emissions inventory methods: A systematic review, Environ. Impact Assess. Rev., 80, 106316, https://doi.org/10.1016/j.eiar.2019.106316, 2020.

Babenhauserheide, A., Hase, F., and Morino, I.: Net CO_2 fossil fuel emissions of Tokyo estimated directly from measurements of the Tsukuba TCCON site and radiosondes, Atmospheric Meas. Tech., 13, 2697–2710, https://doi.org/10.5194/amt-13-2697-2020, 2020.

Barkley, Z., Davis, K., Miles, N., Richardson, S., Deng, A., Hmiel, B., Lyon, D., and Lauvaux, T.: Quantification of oil and gas methane emissions in the Delaware and Marcellus basins using a network of continuous tower-based measurements, Atmospheric Chem. Phys., 23, 6127–6144, https://doi.org/10.5194/acp-23-6127-2023, 2023.

Bisht, J. S. H., Patra, P. K., Takigawa, M., Kanaya, Y., Yamaguchi, M., Machida, T., and Tanimoto, H.: CO_2 high-resolution simulation using WRF-GHG over the Kanto region in Japan, https://doi.org/10.22541/essoar.168626399.94131688/v1, 8 June 2023.

Bisht, J. S. H., Patra, P. K., Takigawa, M., Kanaya, Y., Yamaguchi, M., Machida, T., and Tanimoto, H.: High-Resolution Simulation of CO_2 Using WRF-GHG Over the Kanto Region in Japan, J. Geophys. Res. Atmospheres, 130, e2025JD043589, https://doi.org/10.1029/2025JD043589, 2025.

Brunner, D., Kuhlmann, G., Marshall, J., Clément, V., Fuhrer, O., Broquet, G., Löscher, A., and Meijer, Y.: Accounting for the vertical distribution of emissions in atmospheric CO_2 simulations, Atmospheric Chem. Phys., 19, 4541–4559, https://doi.org/10.5194/acp-19-4541-2019, 2019.

https://doi.org/10.5194/egusphere-2026-2178
Preprint. Discussion started: 21 July 2026

Callewaert, S., Zhou, M., Langerock, B., Wang, P., Wang, T., Mahieu, E., and De Mazière, M.: A WRF-Chem study of the greenhouse gas column and in situ surface concentrations observed in Xianghe, China – Part 1: Methane (CH_4), Atmospheric Chem. Phys., 25, 9519–9544, https://doi.org/10.5194/acp-25-9519-2025, 2025.

Chatani, S., Okumura, M., Shimadera, H., Yamaji, K., Kitayama, K., and Matsunaga, S. N.: Effects of a Detailed Vegetation Database on Simulated Meteorological Fields, Biogenic VOC Emissions, and Ambient Pollutant Concentrations over Japan, Atmosphere, 9, https://doi.org/10.3390/atmos9050179, 2018.

Che, K., Lauvaux, T., Taquet, N., Stremme, W., Xu, Y., Alberti, C., Lopez, M., García-Reynoso, A., Ciais, P., Liu, Y., Ramonet, M., and Grutter, M.: CO_2 Emissions Estimate From Mexico City Using Ground- and Space-Based Remote Sensing, J. Geophys. Res. Atmospheres, 129, e2024JD041297, https://doi.org/10.1029/2024JD041297, 2024a.

Che, K., Lauvaux, T., Taquet, N., Stremme, W., Xu, Y., Alberti, C., Lopez, M., García-Reynoso, A., Ciais, P., Liu, Y., Ramonet, M., and Grutter, M.: Urban XCO_2 Gradients From a Dense Network of Solar Absorption Spectrometers and OCO-3 Over Mexico City, J. Geophys. Res. Atmospheres, 129, e2023JD040063, https://doi.org/10.1029/2023JD040063, 2024b.

Chen, J., Zhao, F., Zeng, N., and Oda, T.: Comparing a global high-resolution downscaled fossil fuel CO_2 emission dataset to local inventory-based estimates over 14 global cities, Carbon Balance Manag., 15, 9, https://doi.org/10.1186/s13021-020-00146-3, 2020.

Chevallier, F., Ciais, P., Conway, T. J., Aalto, T., Anderson, B. E., Bousquet, P., Brunke, E. G., Ciattaglia, L., Esaki, Y., Fröhlich, M., Gomez, A., Gomez-Pelaez, A. J., Haszpra, L., Krummel, P. B., Langenfelds, R. L., Leuenberger, M., Machida, T., Maignan, F., Matsueda, H., Morguí, J. A., Mukai, H., Nakazawa, T., Peylin, P., Ramonet, M., Rivier, L., Sawa, Y., Schmidt, M., Steele, L. P., Vay, S. A., Vermeulen, A. T., Wofsy, S., and Worthy, D.: CO_2 surface fluxes at grid point scale estimated from a global 21 year reanalysis of atmospheric measurements, J. Geophys. Res. Atmospheres, 115, https://doi.org/10.1029/2010JD013887, 2010.

Copernicus Atmosphere Monitoring Service: CAMS global inversion-optimised greenhouse gas fluxes and concentrations (V23r3), https://doi.org/10.24381/ed2851d2, 2020.

Crippa, M., Guizzardi, D., Pisoni, E., Solazzo, E., Guion, A., Muntean, M., Florczyk, A., Schiavina, M., Melchiorri, M., and Hutfilter, A. F.: Global anthropogenic emissions in urban areas: patterns, trends, and challenges, Environ. Res. Lett., 16, 074033, https://doi.org/10.1088/1748-9326/ac00e2, 2021.

Crippa, M., Guizzardi, D., Schaaf, E., Monforti-Ferrario, F., Quadrelli, R., Risquez Martin, A., Rossi, S., Vignati, E., Muntean, M., Brandao De Melo, J., Oom, D., Pagani, F., Banja, M., Taghavi-Moharamli, P., Köykkä, J., Grassi, G., Branco, A., and San-Miguel, J.: GHG emissions of all world countries - 2023 Report, Publications Office of the European Union, https://doi.org/10.2760/953322, 2023.

Dou, X., Wang, Y., Ciais, P., Chevallier, F., Davis, S. J., Crippa, M., Janssens-Maenhout, G., Guizzardi, D., Solazzo, E., Yan, F., Huo, D., Zheng, B., Zhu, B., Cui, D., Ke, P., Sun, T., Wang, H., Zhang, Q., Gentine, P., Deng, Z., and Liu, Z.: Near-real-time global gridded daily CO_2 emissions, The Innovation, 3, 100182, https://doi.org/10.1016/j.xinn.2021.100182, 2022.

Feng, S., Lauvaux, T., Newman, S., Rao, P., Ahmadov, R., Deng, A., Díaz-Isaac, L. I., Duren, R. M., Fischer, M. L., Gerbig, C., Gurney, K. R., Huang, J., Jeong, S., Li, Z., Miller, C. E., O'Keeffe, D., Patarasuk, R., Sander, S. P., Song, Y., Wong, K. W., and Yung, Y. L.: Los Angeles megacity: a high-resolution land–atmosphere modelling system for urban CO_2 emissions, Atmospheric Chem. Phys., 16, 9019–9045, https://doi.org/10.5194/acp-16-9019-2016, 2016.

Feng, S., Jiang, F., Wang, H., Liu, Y., He, W., Wang, H., Shen, Y., Zhang, L., Jia, M., Ju, W., and Chen, J. M.: China's Fossil Fuel CO_2 Emissions Estimated Using Surface Observations of Coemitted NO_2, Environ. Sci. Technol., 58, 8299–8312, https://doi.org/10.1021/acs.est.3c07756, 2024.

Ferrario, F. M., Crippa, M., Guizzardi, D., Muntean, M., Schaaf, E., Vullo, E. L., Solazzo, E., Olivier, J., and Vignati, E.: EDGAR v6.0 Greenhouse Gas Emissions, 2021.

Friedlingstein, P., O'Sullivan, M., Jones, M. W., Andrew, R. M., Gregor, L., Hauck, J., Le Quéré, C., Luijkx, I. T., Olsen, A., Peters, G. P., Peters, W., Pongratz, J., Schwingshackl, C., Sitch, S., Canadell, J. G., Ciais, P., Jackson, R. B., Alin, S. R., Alkama, R., Arneth, A., Arora, V. K., Bates, N. R., Becker, M., Bellouin, N., Bittig, H. C., Bopp, L., Chevallier, F., Chini, L. P., Cronin, M., Evans, W., Falk, S., Feely, R. A., Gasser, T., Gehlen, M., Gkritzalis, T., Gloege, L., Grassi, G., Gruber, N., Gürses, Ö., Harris, I., Hefner, M., Houghton, R. A., Hurtt, G. C., Iida, Y., Ilyina, T., Jain, A. K., Jersild, A., Kadono, K., Kato, E., Kennedy, D., Klein Goldewijk, K., Knauer, J., Korsbakken, J. I., Landschützer, P., Lefèvre, N., Lindsay, K., Liu, J., Liu, Z., Marland, G., Mayot, N., McGrath, M. J., Metzl, N., Monacci, N. M., Munro, D. R., Nakaoka, S.-I., Niwa, Y., O'Brien, K., Ono, T., Palmer, P. I., Pan, N., Pierrot, D., Pocock, K., Poulter, B., Resplandy, L., Robertson, E., Rödenbeck, C., Rodriguez, C., Rosan, T. M., Schwinger, J., Séférian, R., Shutler, J. D., Skjelvan, I., Steinhoff, T., Sun, Q., Sutton, A. J., Sweeney, C.,

https://doi.org/10.5194/egusphere-2026-2178
Preprint. Discussion started: 21 July 2026

Takao, S., Tanhua, T., Tans, P. P., Tian, X., Tian, H., Tilbrook, B., Tsujino, H., Tubiello, F., van der Werf, G. R., Walker, A. P., Wanninkhof, R., Whitehead, C., Willstrand Wranne, A., et al.: Global Carbon Budget 2022, Earth Syst. Sci. Data, 14, 4811–4900, https://doi.org/10.5194/essd-14-4811-2022, 2022.

Friedlingstein, P., O'Sullivan, M., Jones, M. W., Andrew, R. M., Bakker, D. C. E., Hauck, J., Landschützer, P., Le Quéré, C., Luijkx, I. T., Peters, G. P., Peters, W., Pongratz, J., Schwingshackl, C., Sitch, S., Canadell, J. G., Ciais, P., Jackson, R. B., Alin, S. R., Anthoni, P., Barbero, L., Bates, N. R., Becker, M., Bellouin, N., Decharme, B., Bopp, L., Brasika, I. B. M., Cadule, P., Chamberlain, M. A., Chandra, N., Chau, T.-T.-T., Chevallier, F., Chini, L. P., Cronin, M., Dou, X., Enyo, K., Evans, W., Falk, S., Feely, R. A., Feng, L., Ford, D. J., Gasser, T., Ghattas, J., Gkritzalis, T., Grassi, G., Gregor, L., Gruber, N., Gürses, Ö., Harris, I., Hefner, M., Heinke, J., Houghton, R. A., Hurtt, G. C., Iida, Y., Ilyina, T., Jacobson, A. R., Jain, A., Jarníková, T., Jersild, A., Jiang, F., Jin, Z., Joos, F., Kato, E., Keeling, R. F., Kennedy, D., Klein Goldewijk, K., Knauer, J., Korsbakken, J. I., Körtzinger, A., Lan, X., Lefèvre, N., Li, H., Liu, J., Liu, Z., Ma, L., Marland, G., Mayot, N., McGuire, P. C., McKinley, G. A., Meyer, G., Morgan, E. J., Munro, D. R., Nakaoka, S.-I., Niwa, Y., O'Brien, K. M., Olsen, A., Omar, A. M., Ono, T., Paulsen, M., Pierrot, D., Pocock, K., Poulter, B., Powis, C. M., Rehder, G., Resplandy, L., Robertson, E., Rödenbeck, C., Rosan, T. M., Schwinger, J., Séférian, R., et al.: Global Carbon Budget 2023, Earth Syst. Sci. Data, 15, 5301–5369, https://doi.org/10.5194/essd-15-5301-2023, 2023.

Gately, C. K. and Hutyra, L. R.: Large Uncertainties in Urban-Scale Carbon Emissions, J. Geophys. Res. Atmospheres, 122, 11,242-11,260, https://doi.org/10.1002/2017JD027359, 2017.

Geng, G., Zhang, Q., Martin, R. V., Lin, J., Huo, H., Zheng, B., Wang, S., and He, K.: Impact of spatial proxies on the representation of bottom-up emission inventories: A satellite-based analysis, Atmospheric Chem. Phys., 17, 4131–4145, https://doi.org/10.5194/acp-17-4131-2017, 2017.

Guevara, M., Jorba, O., Tena, C., Denier van der Gon, H., Kuenen, J., Elguindi, N., Darras, S., Granier, C., and Pérez García-Pando, C.: Copernicus Atmosphere Monitoring Service TEMPOral profiles (CAMS-TEMPO): global and European emission temporal profile maps for atmospheric chemistry modelling, Earth Syst. Sci. Data, 13, 367–404, https://doi.org/10.5194/essd-13-367-2021, 2021.

Gurney, K. R., Liang, J., Roest, G., Song, Y., Mueller, K., and Lauvaux, T.: Under-reporting of greenhouse gas emissions in U.S. cities, Nat. Commun., 12, 553, https://doi.org/10.1038/s41467-020-20871-0, 2021.

Han, P., Zeng, N., Oda, T., Zhang, W., Lin, X., Liu, D., Cai, Q., Ma, X., Meng, W., Wang, G., Wang, R., and Zheng, B.: A city-level comparison of fossil-fuel and industry processes-induced CO_2 emissions over the Beijing-Tianjin-Hebei region from eight emission inventories, Carbon Balance Manag., 15, 25, https://doi.org/10.1186/s13021-020-00163-2, 2020a.

Han, P., Lin, X., Zeng, N., Oda, T., Zhang, W., Liu, D., Cai, Q., Crippa, M., Guan, D., Ma, X., Janssens-Maenhout, G., Meng, W., Shan, Y., Tao, S., Wang, G., Wang, H., Wang, R., Wu, L., Zhang, Q., Zhao, F., and Zheng, B.: Province-level fossil fuel CO_2 emission estimates for China based on seven inventories, J. Clean. Prod., 277, 123377, https://doi.org/10.1016/j.jclepro.2020.123377, 2020b.

Iacono, M. J., Delamere, J. S., Mlawer, E. J., Shephard, M. W., Clough, S. A., and Collins, W. D.: Radiative forcing by long-lived greenhouse gases: Calculations with the AER radiative transfer models, J. Geophys. Res. Atmospheres, 113, https://doi.org/10.1029/2008JD009944, 2008.

IEA, P.: World energy outlook 2022, Paris Fr. Int. Energy Agency IEA, 2022.

Iida, Y., Takatani, Y., Kojima, A., and Ishii, M.: Global trends of ocean CO_2 sink and ocean acidification: an observation-based reconstruction of surface ocean inorganic carbon variables, J. Oceanogr., 77, 323–358, https://doi.org/10.1007/s10872-020-00571-5, 2021.

IPCC: Climate Change 2021: The Physical Science Basis. Contribution of Working Group I to the Sixth Assessment Report of the Intergovernmental Panel on Climate Change, Cambridge University Press, Cambridge, United Kingdom and New York, NY, USA, 2021.

Ishidoya, S., Sugawara, H., Terao, Y., Kaneyasu, N., Aoki, N., Tsuboi, K., and Kondo, H.: O_2 : CO_2 exchange ratio for net turbulent flux observed in an urban area of Tokyo, Japan, and its application to an evaluation of anthropogenic CO_2 emissions, Atmospheric Chem. Phys., 20, 5293–5308, https://doi.org/10.5194/acp-20-5293-2020, 2020.

Itoh, S., Kasai, A., Takeshige, A., Zenimoto, K., Kimura, S., Suzuki, K. W., Miyake, Y., Funahashi, T., Yamashita, Y., and Watanabe, Y.: Circulation and haline structure of a microtidal bay in the Sea of Japan influenced by the winter monsoon and the Tsushima Warm Current, J. Geophys. Res. Oceans, 121, 6331–6350, https://doi.org/10.1002/2015JC011441, 2016.

https://doi.org/10.5194/egusphere-2026-2178
Preprint. Discussion started: 21 July 2026

Janardanan, R., Maksyutov, S., Oda, T., Saito, M., Kaiser, J. W., Ganshin, A., Stohl, A., Matsunaga, T., Yoshida, Y., and Yokota, T.: Comparing GOSAT observations of localized CO_2 enhancements by large emitters with inventory-based estimates, Geophys. Res. Lett., 43, 3486–3493, https://doi.org/10.1002/2016GL067843, 2016.

Janjić, Z. I.: The Step-Mountain Eta Coordinate Model: Further Developments of the Convection, Viscous Sublayer, and Turbulence Closure Schemes, Mon. Weather Rev., 122, 927–945, https://doi.org/10.1175/1520-0493(1994)122%3C0927:TSMECM%3E2.0.CO;2, 1994.

Janssens-Maenhout, G., Crippa, M., Guizzardi, D., Muntean, M., Schaaf, E., Dentener, F., Bergamaschi, P., Pagliari, V., Olivier, J. G. J., Peters, J. A. H. W., van Aardenne, J. A., Monni, S., Doering, U., Petrescu, A. M. R., Solazzo, E., and Oreggioni, G. D.: EDGAR v4.3.2 Global Atlas of the three major greenhouse gas emissions for the period 1970–2012, Earth Syst. Sci. Data, 11, 959–1002, https://doi.org/10.5194/essd-11-959-2019, 2019.

Japan Meteorological Agency: Outline of the Operational Numerical Weather Prediction at the Japan Meteorological Agency, 2019.

Johansson, L., Jalkanen, J.-P., and Kukkonen, J.: Global assessment of shipping emissions in 2015 on a high spatial and temporal resolution, Atmos. Environ., 167, 403–415, https://doi.org/10.1016/j.atmosenv.2017.08.042, 2017.

Jones, M. W., Andrew, R. M., Peters, G. P., Janssens-Maenhout, G., De-Gol, A. J., Ciais, P., Patra, P. K., Chevallier, F., and Le Quéré, C.: Gridded fossil CO_2 emissions and related O_2 combustion consistent with national inventories 1959–2018, Sci. Data, 8, 2, https://doi.org/10.1038/s41597-020-00779-6, 2021.

Kain, J. S.: The Kain–Fritsch Convective Parameterization: An Update, J. Appl. Meteorol., 43, 170–181, https://doi.org/10.1175/1520-0450(2004)043%3C0170:TKCPAU%3E2.0.CO;2, 2004.

Karion, A., Lopez-Coto, I., Gourdji, S. M., Mueller, K., Ghosh, S., Callahan, W., Stock, M., DiGangi, E., Prinzivalli, S., and Whetstone, J.: Background conditions for an urban greenhouse gas network in the Washington, DC, and Baltimore metropolitan region, Atmospheric Chem. Phys., 21, 6257–6273, https://doi.org/10.5194/acp-21-6257-2021, 2021.

Kiel, M., Eldering, A., Roten, D. D., Lin, J. C., Feng, S., Lei, R., Lauvaux, T., Oda, T., Roehl, C. M., Blavier, J.-F., and Iraci, L. T.: Urban-focused satellite CO_2 observations from the Orbiting Carbon Observatory-3: A first look at the Los Angeles megacity, Remote Sens. Environ., 258, 112314, https://doi.org/10.1016/j.rse.2021.112314, 2021.

Kim, J., Berelson, W. M., Rollins, N. E., Asimow, N. G., Newman, C., Cohen, R. C., Miller, J. B., McDonald, B. C., Peischl, J., and Lehman, S. J.: Observing Anthropogenic and Biogenic CO_2 Emissions in Los Angeles Using a Dense Sensor Network, Environ. Sci. Technol., 59, 3508–3517, https://doi.org/10.1021/acs.est.4c11392, 2025.

Lauvaux, T., Schuh, A. E., Uliasz, M., Richardson, S., Miles, N., Andrews, A. E., Sweeney, C., Diaz, L. I., Martins, D., Shepson, P. B., and Davis, K. J.: Constraining the CO_2 budget of the corn belt: exploring uncertainties from the assumptions in a mesoscale inverse system, Atmospheric Chem. Phys., 12, 337–354, https://doi.org/10.5194/acp-12-337-2012, 2012.

Lauvaux, T., Miles, N. L., Deng, A., Richardson, S. J., Cambaliza, M. O., Davis, K. J., Gaudet, B., Gurney, K. R., Huang, J., O'Keefe, D., Song, Y., Karion, A., Oda, T., Patarasuk, R., Razlivanov, I., Sarmiento, D., Shepson, P., Sweeney, C., Turnbull, J., and Wu, K.: High-resolution atmospheric inversion of urban CO_2 emissions during the dormant season of the Indianapolis Flux Experiment (INFLUX), J. Geophys. Res. Atmospheres, 121, 5213–5236, https://doi.org/10.1002/2015JD024473, 2016.

Lauvaux, T., Gurney, K. R., Miles, N. L., Davis, K. J., Richardson, S. J., Deng, A., Nathan, B. J., Oda, T., Wang, J. A., Hutyra, L., and Turnbull, J.: Policy-Relevant Assessment of Urban CO_2 Emissions, Environ. Sci. Technol., 54, 10237–10245, https://doi.org/10.1021/acs.est.0c00343, 2020.

Lian, J., Bréon, F.-M., Broquet, G., Zaccheo, T. S., Dobler, J., Ramonet, M., Staufer, J., Santaren, D., Xueref-Remy, I., and Ciais, P.: Analysis of temporal and spatial variability of atmospheric CO_2 concentration within Paris from the GreenLITE™ laser imaging experiment, Atmospheric Chem. Phys., 19, 13809–13825, https://doi.org/10.5194/acp-19-13809-2019, 2019.

Lian, J., Lauvaux, T., Utard, H., Bréon, F.-M., Broquet, G., Ramonet, M., Laurent, O., Albarus, I., Cucchi, K., and Ciais, P.: Assessing the Effectiveness of an Urban CO_2 Monitoring Network over the Paris Region through the COVID-19 Lockdown Natural Experiment, Environ. Sci. Technol., 56, 2153–2162, https://doi.org/10.1021/acs.est.1c04973, 2022.

Lian, J., Lauvaux, T., Utard, H., Bréon, F.-M., Broquet, G., Ramonet, M., Laurent, O., Albarus, I., Chariot, M., Kotthaus, S., Haeffelin, M., Sanchez, O., Perrussel, O., Denier van der Gon, H. A., Dellaert, S. N. C., and Ciais, P.: Can we use atmospheric CO_2 measurements to verify emission trends reported by cities? Lessons from a 6-year atmospheric inversion over Paris, Atmospheric Chem. Phys., 23, 8823–8835, https://doi.org/10.5194/acp-23-8823-2023, 2023.

https://doi.org/10.5194/egusphere-2026-2178
Preprint. Discussion started: 21 July 2026

Lian, J., Laurent, O., Chariot, M., Lienhardt, L., Ramonet, M., Utard, H., Lauvaux, T., Bréon, F.-M., Broquet, G., Cucchi, K., Millair, L., and Ciais, P.: Development and deployment of a mid-cost CO_2 sensor monitoring network to support atmospheric inverse modeling for quantifying urban CO_2 emissions in Paris, Atmospheric Meas. Tech., 17, 5821–5839, https://doi.org/10.5194/amt-17-5821-2024, 2024.

Liotta, C., Viguié, V., and Creutzig, F.: Environmental and welfare gains via urban transport policy portfolios across 120 cities, Nat. Sustain., 6, 1067–1076, https://doi.org/10.1038/s41893-023-01138-0, 2023.

Liu, X., Xu, H., and Zhang, M.: The effects of urban expansion on carbon emissions: Based on the spatial interaction and transmission mechanism, J. Clean. Prod., 434, 140019, https://doi.org/10.1016/j.jclepro.2023.140019, 2024.

Liu, Z., Ciais, P., Deng, Z., Davis, S. J., Zheng, B., Wang, Y., Cui, D., Zhu, B., Dou, X., Ke, P., Sun, T., Guo, R., Zhong, H., Boucher, O., Bréon, F.-M., Lu, C., Guo, R., Xue, J., Boucher, E., Tanaka, K., and Chevallier, F.: Carbon Monitor, a near-real-time daily dataset of global CO_2 emission from fossil fuel and cement production, Sci. Data, 7, 392, https://doi.org/10.1038/s41597-020-00708-7, 2020.

Machida, T., Tohjima, Y., Katsumata, K., and Mukai, H.: A new CO_2 calibration scale based on gravimetric one-step dilution cylinders in National Institute for Environmental Studies-NIES 09 CO_2 scale, in: 15th WMO/IAEA Meeting of Experts on Carbon Dioxyide, other Greenhouse Gases and Related Tracers Measurement Techniques, 165–169, 2011.

Mahadevan, P., Wofsy, S. C., Matross, D. M., Xiao, X., Dunn, A. L., Lin, J. C., Gerbig, C., Munger, J. W., Chow, V. Y., and Gottlieb, E. W.: A satellite-based biosphere parameterization for net ecosystem CO_2 exchange: Vegetation Photosynthesis and Respiration Model (VPRM), Glob. Biogeochem. Cycles, 22, https://doi.org/10.1029/2006GB002735, 2008.

Martin, C. R., Zeng, N., Karion, A., Mueller, K., Ghosh, S., Lopez-Coto, I., Gurney, K. R., Oda, T., Prasad, K., Liu, Y., Dickerson, R. R., and Whetstone, J.: Investigating sources of variability and error in simulations of carbon dioxide in an urban region, Atmos. Environ., 199, 55–69, https://doi.org/10.1016/j.atmosenv.2018.11.013, 2019.

McKain, K., Wofsy, S. C., Nehrkorn, T., Eluszkiewicz, J., Ehleringer, J. R., and Stephens, B. B.: Assessment of ground-based atmospheric observations for verification of greenhouse gas emissions from an urban region, Proc. Natl. Acad. Sci., 109, 8423–8428, https://doi.org/10.1073/pnas.1116645109, 2012.

Nakajima, K., Takahashi, H., Yokoyama, H., and Tsunematsu, N.: Vertical Structures of Nocturnal Potential Temperature under Clear and Weak Wind Conditions in the Central Urban Area of Tokyo, Japan: Statistical Analysis Using Observation Data at Tokyo Tower, Geogr. Rev. Jpn. Ser. A, 91, 24–42, https://doi.org/10.4157/grj.91.24, 2018.

NCEP: NCEP GDAS/FNL 0.25 Degree Global Tropospheric Analyses and Forecast Grids, NSF National Center for Atmospheric Research, https://doi.org/10.5065/D65Q4T4Z, 2015.

Nerobelov, G. M., Timofeyev, Yu. M., Smyshlyaev, S. P., Foka, S. Ch., and Imhasin, H. H.: Comparison of CO_2 Content in the Atmosphere of St. Petersburg According to Numerical Modeling and Observations, Izv. Atmospheric Ocean. Phys., 59, 275–286, https://doi.org/10.1134/S0001433823020056, 2023.

Nomura, S., Mukai, H., Terao, Y., Machida, T., and Nojiri, Y.: Six years of atmospheric CO_2 observations at Mt. Fuji recorded with a battery-powered measurement system, Atmospheric Meas. Tech., 10, 667–680, https://doi.org/10.5194/amt-10-667-2017, 2017.

Oda, T. and Maksyutov, S.: ODIAC Fossil Fuel CO_2 Emissions Dataset (ODIAC2023), https://doi.org/10.17595/20170411.001, 2015.

Oda, T., Maksyutov, S., and Andres, R. J.: The Open-source Data Inventory for Anthropogenic CO_2, version 2016 (ODIAC2016): a global monthly fossil fuel CO_2 gridded emissions data product for tracer transport simulations and surface flux inversions, Earth Syst. Sci. Data, 10, 87–107, https://doi.org/10.5194/essd-10-87-2018, 2018.

Oda, T., Bun, R., Kinakh, V., Topylko, P., Halushchak, M., Marland, G., Lauvaux, T., Jonas, M., Maksyutov, S., Nahorski, Z., Lesiv, M., Danylo, O., and Horabik-Pyzel, J.: Errors and uncertainties in a gridded carbon dioxide emissions inventory, Mitig. Adapt. Strateg. Glob. Change, 24, 1007–1050, https://doi.org/10.1007/s11027-019-09877-2, 2019.

Ohyama, H., Frey, M. M., Morino, I., Shiomi, K., Nishihashi, M., Miyauchi, T., Yamada, H., Saito, M., Wakasa, M., Blumenstock, T., and Hase, F.: Anthropogenic CO_2 emission estimates in the Tokyo metropolitan area from ground-based CO_2 column observations, Atmospheric Chem. Phys., 23, 15097–15119, https://doi.org/10.5194/acp-23-15097-2023, 2023.

https://doi.org/10.5194/egusphere-2026-2178
Preprint. Discussion started: 21 July 2026

O'Rourke, P. R., Smith, S. J., Mott, A., Ahsan, H., McDuffie, E. E., Crippa, M., Klimont, Z., McDonald, B., Wang, S., Nicholson, M. B., Feng, L., and Hoesly, R. M.: CEDS v_2021_04_21 Release Emission Data, https://doi.org/10.5281/zenodo.4737769, 2021.

Ribeiro, H. V., Rybski, D., and Kropp, J. P.: Effects of changing population or density on urban carbon dioxide emissions, Nat. Commun., 10, 3204, https://doi.org/10.1038/s41467-019-11184-y, 2019.

Saito, M., Yamada, H., and Oda, T.: A high-resolution spatially explicit emission inventory of fossil fuel CO_2 emissions from Japan, ICOS Science Conference 2022, 118, 2022.

Sargent, M., Barrera, Y., Nehrkorn, T., Hutyra, L. R., Gately, C. K., Jones, T., McKain, K., Sweeney, C., Hegarty, J., Hardiman, B., Wang, J. A., and Wofsy, S. C.: Anthropogenic and biogenic CO_2 fluxes in the Boston urban region, Proc. Natl. Acad. Sci., 115, 7491–7496, https://doi.org/10.1073/pnas.1803715115, 2018.

Smirnova, T. G., Brown, J. M., Benjamin, S. G., and Kenyon, J. S.: Modifications to the Rapid Update Cycle Land Surface Model (RUC LSM) Available in the Weather Research and Forecasting (WRF) Model, Mon. Weather Rev., 144, 1851–1865, https://doi.org/10.1175/MWR-D-15-0198.1, 2016.

Soulie, A., Granier, C., Darras, S., Zilbermann, N., Doumbia, T., Guevara, M., Jalkanen, J.-P., Keita, S., Liousse, C., Crippa, M., Guizzardi, D., Hoesly, R., and Smith, S. J.: Global anthropogenic emissions (CAMS-GLOB-ANT) for the Copernicus Atmosphere Monitoring Service simulations of air quality forecasts and reanalyses, Earth Syst. Sci. Data, 16, 2261–2279, https://doi.org/10.5194/essd-16-2261-2024, 2024.

Sugawara, H., Ishidoya, S., Terao, Y., Takane, Y., Kikegawa, Y., and Nakajima, K.: Anthropogenic CO_2 Emissions Changes in an Urban Area of Tokyo, Japan, Due to the COVID-19 Pandemic: A Case Study During the State of Emergency in April–May 2020, Geophys. Res. Lett., 48, e2021GL092600, https://doi.org/10.1029/2021GL092600, 2021.

Taquet, N., Stremme, W., González del Castillo, M. E., Almanza, V., Bezanilla, A., Laurent, O., Alberti, C., Hase, F., Ramonet, M., Lauvaux, T., Che, K., and Grutter, M.: CO_2 and CO temporal variability over Mexico City from ground-based total column and surface measurements, Atmospheric Chem. Phys., 24, 11823–11848, https://doi.org/10.5194/acp-24-11823-2024, 2024.

Thompson, G., Field, P. R., Rasmussen, R. M., and Hall, W. D.: Explicit Forecasts of Winter Precipitation Using an Improved Bulk Microphysics Scheme. Part II: Implementation of a New Snow Parameterization, Mon. Weather Rev., 136, 5095–5115, https://doi.org/10.1175/2008MWR2387.1, 2008.

Thorpe, A. K., Green, R. O., Thompson, D. R., Brodrick, P. G., Chapman, J. W., Elder, C. D., Irakulis-Loitxate, I., Cusworth, D. H., Ayasse, A. K., Duren, R. M., Frankenberg, C., Guanter, L., Worden, J. R., Dennison, P. E., Roberts, D. A., Chadwick, K. D., Eastwood, M. L., Fahlen, J. E., and Miller, C. E.: Attribution of individual methane and carbon dioxide emission sources using EMIT observations from space, Sci. Adv., 9, eadh2391, https://doi.org/10.1126/sciadv.adh2391, 2023.

Ueyama, M., Takao, Y., Yazawa, H., Tanaka, M., Yabuki, H., Kumagai, T., Iwata, H., Awal, Md. A., Du, M., Harazono, Y., Hata, Y., Hirano, T., Hiura, T., Ide, R., Ishida, S., Ishikawa, M., Kitamura, K., Kominami, Y., Komiya, S., Kotani, A., Inoue, Y., Machimura, T., Matsumoto, K., Matsuura, Y., Mizoguchi, Y., Murayama, S., Nagano, H., Nakai, T., Nakaji, T., Nakaya, K., Ohkubo, S., Ohta, T., Ono, K., Saitoh, T. M., Sakabe, A., Shimizu, T., Shimoda, S., Sugita, M., Takagi, K., Takahashi, Y., Takamura, N., Takanashi, S., Takimoto, T., Yasuda, Y., Wang, Q., Asanuma, J., Hasegawa, H., Hiyama, T., Iijima, Y., Ishidoya, S., Itoh, M., Kato, T., Kondo, H., Kosugi, Y., Kume, T., Maeda, T., Matsuura, S., Maximov, T., Miyama, T., Moriwaki, R., Muraoka, H., Petrov, R., Suzuki, J., Taniguchi, S., and Ichii, K.: The JapanFlux2024 dataset for eddy covariance observations covering Japan and East Asia from 1990 to 2023, Earth Syst. Sci. Data, 17, 3807–3833, https://doi.org/10.5194/essd-17-3807-2025, 2025.

Vardag, S. N. and Maiwald, R.: Optimising urban measurement networks for CO_2 flux estimation: a high-resolution observing system simulation experiment using GRAMM/GRAL, Geosci. Model Dev., 17, 1885–1902, https://doi.org/10.5194/gmd-17-1885-2024, 2024.

Winkler, L., Pearce, D., Nelson, J., and Babacan, O.: The effect of sustainable mobility transition policies on cumulative urban transport emissions and energy demand, Nat. Commun., 14, 2357, https://doi.org/10.1038/s41467-023-37728-x, 2023.

WMO: GAW Report No. 275: IG3IS Urban Greenhouse Gas Emission Observation and Monitoring Good Research Practice Guidelines, WMO, Geneva, 2022.

WMO: GAW Report No. 314: Integrated Global Greenhouse Gas Information System: Urban Emission Observation and Monitoring Good Research Practice Guidelines, WMO, Geneva, https://doi.org/10.59327/WMO/GAW/314, 2025.

https://doi.org/10.5194/egusphere-2026-2178
Preprint. Discussion started: 21 July 2026

Yamada, K., Niwa, Y., Terao, Y., Tohjima, Y., Tsuboi, K., Ishijima, K., and Murayama, S.: Estimation of CO_2 Fluxes from Tokyo Using a Global Model and Tower Observation, J. Meteorol. Soc. Jpn. Ser II, 103, 67–85, https://doi.org/10.2151/jmsj.2025-004, 2025.

Yang, E. G., Kort, E. A., Wu, D., Lin, J. C., Oda, T., Ye, X., and Lauvaux, T.: Using Space-Based Observations and Lagrangian Modeling to Evaluate Urban Carbon Dioxide Emissions in the Middle East, J. Geophys. Res. Atmospheres, 125, e2019JD031922, https://doi.org/10.1029/2019JD031922, 2020.

Yap, W., Wu, A. N., Miller, C., and Biljecki, F.: Revealing building operating carbon dynamics for multiple cities, Nat. Sustain., 8, 1199–1210, https://doi.org/10.1038/s41893-025-01615-8, 2025.

Zhao, X., Chen, J., Marshall, J., Gałkowski, M., Hachinger, S., Dietrich, F., Shekhar, A., Gensheimer, J., Wenzel, A., and Gerbig, C.: Understanding greenhouse gas (GHG) column concentrations in Munich using the Weather Research and Forecasting (WRF) model, Atmospheric Chem. Phys., 23, 14325–14347, https://doi.org/10.5194/acp-23-14325-2023, 2023.

Zheng, B., Zhang, Q., Tong, D., Chen, C., Hong, C., Li, M., Geng, G., Lei, Y., Huo, H., and He, K.: Resolution dependence of uncertainties in gridded emission inventories: a case study in Hebei, China, Atmospheric Chem. Phys., 17, 921–933, https://doi.org/10.5194/acp-17-921-2017, 2017.